ELECTROCHEMICAL IMPEDANCE SPECTROSCOPY OF ZIRCONIUM

OXIDATION FOR IN-SITU NUCLEAR SENSING APPLICATIONS

by

Michael Andrew Reynolds

A thesis

submitted in partial fulfillment

of the requirements of the degree of

Master of Science in Materials Science and Engineering

Boise State University

May 2022

BOISE STATE UNIVERSITY GRADUATE COLLEGE

DEFENSE COMMITTEE AND FINAL READING APPROVALS

of the thesis submitted by

Michael Andrew Reynolds

Thesis Title: Electrochemical Impedance Spectroscopy of Zirconium Oxidation for In-Situ Nuclear Sensing Applications

Date of Final Oral Examination: 1 July 2021

The following individuals read and discussed the thesis submitted by student Michael Andrew Reynolds, and they evaluated his presentation and response to questions during the final oral examination. They found that the student passed the final oral examination.

Michael Hurley, Ph.D.   Chair, Supervisory Committee

Hui Claire Xiong, Ph.D.   Co-Chair, Supervisory Committee

Hongqiang Hu, Ph.D.   Member, Supervisory Committee

The final reading approval of the thesis was granted by Michael Hurley, Ph.D., Chair of the Supervisory Committee. The thesis was approved by the Graduate College.

DEDICATION

For my past, current, and future family.

ACKNOWLEDGMENTS

ABSTRACT

To meet the ever-growing energy demands of the modern world, alternative forms of producing power are necessary, and the field of nuclear engineering holds promise to answer this call. Nuclear fuel cladding in light water reactors (LWRs) currently draws a large amount of attention from scientists and researchers, as it provides many challenges to design around. Since the 1950s, zirconium and its protective oxide layer have been utilized as an effective material for the task, possessing good mechanical strengths, high corrosion resistance, and a low neutron absorption cross section. Despite these beneficial properties, however, fuel cladding remains vulnerable to several different harmful scenarios. Loss of coolant accidents (LOCAs), waterside corrosion, and hydrogen embrittlement all have the ability to degrade materials performance including the protective oxidation layer on zirconium alloys and jeopardize the integrity of a LWR system. In order to better predict and monitor how zirconium and zirconium alloys behave in the extreme conditions in a light water reactor, studying this oxidation process and developing techniques to monitor its growth in-situ are of high priority.

Electrochemical Impedance Spectroscopy (EIS) is a well-established electrochemical method for non-destructively evaluating materials by inducing an AC perturbation onto the system and observing resultant impedance curves generated from a wide frequency range. Working in conjunction with the Idaho National Laboratory (INL), in-situ EIS was performed on pure zirconium, Zry-4, and Zry-2.65Nb in de-ionized water, LiOH, and KOH at varying temperatures and pressures to gain insight into

zirconium oxide resistivity and impedance, as well as to mimic the in-core reactor operating conditions absent of irradiation. Through equivalent circuit modeling, specific EIS signatures can be determined to better identify the oxide state present in a given system. Utilizing EIS, zirconium alloy degradation can be more readily understood in real time and can support the development of in-core nuclear fuel cladding sensors. Future research surrounding this work will be focused on in-reactor testing to observe how the system reacts under irradiation and sensor packaging for specific reactor test systems.

TABLE OF CONTENTS

LIST OF TABLES

LIST OF FIGURES

CHAPTER 1: INTRODUCTION

Light water reactor (LWR) operating conditions in the nuclear industry present many engineering challenges. In order to increase fuel burn-up and prevent enhanced degradation of critical components, strategic and innovative design criteria must be followed. One such component is nuclear fuel cladding, which serves to encapsulate nuclear fuel during operations. Here, several factors including temperature, primary water chemistry, and residual radiation levels greatly affect its performance, and lead engineers and scientists to select materials that survive in these harsh conditions. Zirconium, with its low neutron absorption cross section, good mechanical properties, and high corrosion resistance, provides a protective oxide layer that serves as a barrier between it and the primary water nuclear fuel cladding resides in. This oxidation prevents uniform corrosion along the outside of the cladding and serves to ensure reactor efficiency and safety. Pure zirconium has been known to have an unstable oxide at elevated temperatures [1], but through adding additional alloying elements oxide stabilization comes more readily. The development of these zirconium alloys has been an area of heavy research since the 1950s [2, 3] for nuclear applications. In general, even low amounts of alloying reduces corrosion issues and helps ensure oxide stability. More recent evolutions of zirconium alloys have increased amounts of Sn and Nb (Zircaloy-4 and Zr-2.65Nb), which also help with hydrogen ingress in the system and other mechanical issues. These alloys have been selected in this study as they are two of the more prominent alloys used in LWRs.

Several environmental circumstances jeopardize zirconium oxide performance, such as loss of coolant accidents, waterside corrosion, and hydrogen pick up. Each of these issues lead to what is known as the "breakaway phenomena", where the oxide begins to crack and degrade, causing hydrogen embrittlement into the bulk zirconium metal [4-6]. This hinders the success of oxide cladding protection and has generated the need for in-situ observation of this material system. Electrochemical impedance spectroscopy (EIS), an electrochemical analysis method with a demonstrated history of studying oxide and corrosion mechanisms, holds promise as a technique for such a task. Implementation of this technique has been widely used to better understand corrosion kinetics and degradation mechanisms of zirconium oxides [7-26], but a comprehensive study surrounding the generated spectra on this specific material system remains to be explored. By being able to categorize and interpret the impedance spectra pulled from these experiments, identifying variables such as alloying, electrolyte, and oxidation state, the overall status and integrity of the oxide can be identified. From a developed understanding of this spectra, it is anticipated that an in-situ electrochemical sensor will be developed, and widely implemented into existing nuclear systems in order to better monitor reactor health, preserve integrity, and increase longevity.

CHAPTER 2: BACKGROUND

2.1 Zirconium Oxidation

Under nominal conditions, the ZrO_2 passive film serves as a protective barrier to the environments presented to it inside LWRs. When exposed to the primary water, subsequent oxidation of the metal is driven by electrode potential differences in the system and allows species to migrate across the native film. The general diffusion mechanism involves the oxygen from the primary water moving to an oxygen vacancy site located at the oxide layer surface, where it is then absorbed. Oxygen anions then reach the oxide-metal interface and react with the Zr cations, forming the oxide. From this oxidation reaction, electrons are released and reduce the protons at the cathode site [1]. These hydrogen ions progressing into the bulk zirconium can cause what is known as hydrogen embrittlement and can result in serious mechanical detriment to the base metal, making it much more brittle. Several studies investigate at depth at the additions of these hydrides into the system [4-6, 27], but this area of material degradation is out of the scope for this current work. The rate limiting step for this process is considered to be the overall transport of these oxygen vacancies following the grain boundaries [18, 28]. Some literature has reported that the overall oxidation kinetics at high temperatures remains very similar for zirconium alloys, regardless of whether it occurs in water, air or steam [29, 30], which holds significance since the oxidation of our zirconium samples was carried out in air in order to generate mass gain curves for each of the specimens.

For this work, we are especially interested in the evolution of this oxide in aqueous solutions, more specifically those of the LWR categories. Deionized water, lithium hydroxide (LiOH), and potassium hydroxide (KOH) are all used as pH controllers added to LWR water chemistry to help maintain corrosion and stability of in-core components, and each of these have been reported to have varying oxidation rates and their own corrosion resistant behaviors [5, 8, 10, 13,.15-18, 20-23].

Structurally, studies have reported a zirconium oxide system that consists of a compact, dense structure, with an outer, more porous layer forming over time [1, 23]. Others consider a more detailed three-layer system, with a semi-porous structure located between the metal/oxide interface and the outer, more porous region that accounts for a gradient progression of porosity [31]. This distinction between oxide structures becomes important when performing data analysis of impedance curves, and the final selection of the equivalent circuit model.

It has been observed, however, that zirconium experiences a relatively unstable corrosion process in lithiated water [32, 33], and generates a cracked and uneven layer above the base metal. With small amounts of Sn or Nb being added, as in the cases of Zircaloy-4 and Zr-2.65Nb, respectively, the growth kinetics are much more stable and make it well suited for nuclear fuel cladding applications. The oxidation state of zirconium is typically divided into two categories, both pre-transition and post-transition, with the oxidation kinetics and oxide thickness defining which transition region the oxide is currently in. This transition is also referred to as the "breakaway phenomena", where the oxide cracks and allows for oxygen and hydrogen species to travel more readily through to the base metal, significantly increasing the corrosion rate. This distinction

between pre and post breakaway status, and to how this breakaway occurs, has been an area of much interest. The pre-transition oxide is generally accepted as approximately 2 microns or thinner (More specifically, 2.2 microns for Zry-4 in PWR water at 360°C [14, 34], and contains the ZrO and the ZrO_2 phases. Once this oxide develops begins to arrive at the post-transition stage, other phases such as ZrO_3 and ω-Zr have been reported to be seen [28]. Several authors additionally have reported an oxygen-rich zone residing close to the metal/oxide interface, [28, 35-38], and consider it a supplemental sub-oxide phase. This oxygen enriched zone was observed for each of the alloy types investigated in this study and is further reported on in this work.

The crystal structure and morphology of the zirconium oxide system has complexities that derive from alloying additions, temperature, as well as the type of aqueous solution it resides in. In the bulk of zirconium samples, primarily the monoclinic phase is observed [39]. At the metal/oxide interface, the tetragonal phase composition can be seen, and in post breakaway samples an increased amount of tetragonal phase is located towards the bulk. Results from works here at Boise State University via Raman Spectroscopy and Scanning Kelvin probe force microscopy (SKPFM) have shown that stress gradients exist between the different phases, as well as lattice mismatch at the metal/oxide interface [40,41]. These compressive forces are believed to contribute to oxide cracking, and once this occurs the kinetics evolve from a parabolic rate law to a more cubic growth rate. Other work stemming from literature additionally reports that these stress gradients that cause the volumetric differences within the oxide are especially exaggerated for that of Zry-4 specimens with increased amounts of Sn [14, 23, 29, 42].

2.2 Impedance Spectroscopy

Electrochemical impedance spectroscopy (EIS) is an assessment method used to explore the dielectric response of an electrochemical cell, and can produce valuable information about oxide thicknesses, corrosion rates, and the nature of the oxide. It is a non-destructive technique that applies an alternating potential to a system and observes the resultant current in the cell, over a specified frequency range. The cell exhibits an impedance response to the applied potential and yields information about the system being studied. EIS data is often displayed with either Bode or Nyquist plots, and used in conjunction with equivalent circuits, they can be modeled and can provide insight to the physical processes occurring in an electrochemical system [7-11, 13-15, 20-24, 26, 27]. Below, in Table 1, the necessary variables to define and describe chosen equivalent circuit models can be seen.

Table 1   Denoted variables for equivalent circuit modeling.

Variable	Symbol
CPE	Constant Phase Element
Y	Young's Impedance
R_s	Solution Resistance
α	CPE Coefficient
ε_0	Vacuum Permittivity
Z_f	Faraday Process on Surface
R_d	Resistance of Dense Layer in Oxide
ε	Dielectric Constant of Oxide Layer
C	Adsorption
R_{ct}	Charge Transfer Resistance
ω	Angular Frequency
R_p	Polarization Resistance
R_o	Oxide Resistance

There are many sources in an electrochemical cell that contribute to the impedance recorded during EIS. The electrolyte used within the cell will contribute an electrolyte resistance that is dependent on cell geometry and solution conductivity, as shown in the equation below.

$$R_S = \frac{l}{k * A}$$

Equation 1: Electrolyte resistance (Rs) under uniform current, with solution conductivity (k), cell area (A), and cell length (l)

Electrochemical reactions between the working electrode and electrolyte will contribute a charge transfer resistance. This resistance is kinetically controlled as shown in the equation below.

$$R_{ct} = \frac{RT}{nFi_0}$$

Equation 2: Charge transfer resistance (R_{ct}) when system is at equilibrium, which depends on the gas constant (R), temperature (T), number of electrons (n), Faraday's constant (F), and exchange current density (i_0)

Similarly, diffusion and mass transfer within the cell generates something known as the "Warburg impedance". This typically manifests at a 45° phase shift on a Bode plot or as a 45° line on a Nyquist plot [14,15]. The equation for Warburg impedance is shown here in Equation 3:

$$Z_w = \frac{1}{\sigma\sqrt{i\omega}}$$

Equation 3: Warburg impedance (Z_w) as it depends on the radial frequency (ω) and the Warburg coefficient (σ) or Warburg capacitance

$$Z_w = \sigma\omega^{-\frac{1}{2}}(1-j) * tanh(\delta(\frac{j\omega}{D})^{-\frac{1}{2}})$$

Equation 4: Warburg impedance (Z_w) for a diffusion layer of finite thickness, which depends on the Warburg coefficient (σ) , radial frequency (ω), Nernst diffusion layer thickness (δ), the $\sqrt{-1}$ (j), and average diffusion coefficient of diffusing species (D)

There are also sources within an electrochemical cell that contribute capacitance during EIS. The interaction between electrodes and ions in solution will produce a double layer of charges. This double layer, also known as the Helmholtz layer, acts as a capacitor and contributes capacitance wherever electrodes are in contact with solution. However, sources that contribute capacitance during EIS rarely act as ideal capacitors. Instead, they behave somewhere amidst a resistor and a capacitor. These are defined as constant phase elements and are represented by the equation below:

$$Z_{CPE} = \frac{1}{(j\omega)^{\alpha}Y_0}$$

Equation 5: Impedance for a constant phase element (Z_{CPE}), with the initial capacitance (Y_0), the $\sqrt{-1}$ (j), and an admittance (α) which is between zero and one. Zero represents a pure resistor, and one represents a pure capacitor. When α equals one half it can represent the Warburg impedance.

Impedance and capacitance sources such as these form the basis for constructing equivalent circuits. Each circuit element used is meant to relate to a specific process occurring within the electrochemical cell. By understanding how the impedance and capacitance of the system relates to one another, as well as the source of each of these

phenomena, one can distinguish multiple processes occurring during the EIS experiment

and draw conclusions from such results.

2.3 Implementation of EIS to study zirconium oxides

EIS has been demonstrated as an efficient way to characterize the zirconium oxide

material system. Several authors have exhibited the ability to predict oxide thickness

growth [7, 11, 15, 25], with others successfully characterizing electrical properties such

as the oxide resistivity and relating it directly to hydrogen pickup fraction [27]. Below in

Figure 1, the proposed circuits used to model the zirconium oxide system are presented.
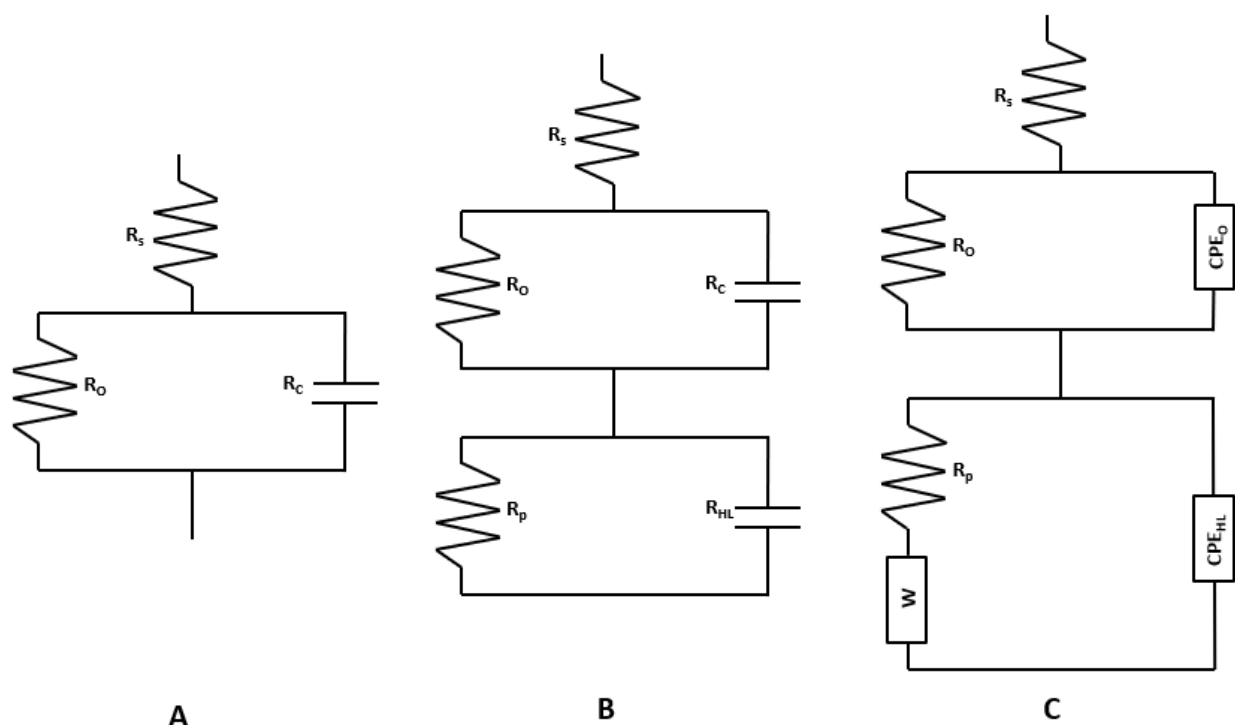
Figure 1   Variations in equivalent circuit. Circuit (a) constitutes zirconium oxide before breakaway and is represented by a basic oxide capacitor and resistor as well as a solution resistance. Circuit (b) shows zirconium oxide after breakaway and includes an extra resistor and capacitor to represent a separate oxide phase. Circuit (c) is an evolution of circuit (b), in which the capacitors are replaced by one or more constant phase elements. Other factors are now included, such as polarization resistance, double layer (Helmholtz) capacitance, and Warburg impedance

Initially, equivalent circuits were modeled using resistive and capacitive elements, as they are a viable way to construct equivalent circuits. However, as established in Equation 5, in real systems sources that contribute capacitance rarely behave as true capacitors. To this end it is common to replace capacitive elements in an equivalent circuit with constant phase elements. These CPEs can replace many of the capacitive elements in an equivalent circuit to better capture the non-ideal behavior of the electrochemical system being represented. The equation for complex capacitance is displayed below.

$$C^* = C_\infty + \frac{B}{(j\omega)^{1-n}}$$

Equation 6: Complex capacitance for an oxide layer, is to relates to the capacitance at infinite frequency (C_∞), the angular frequency (ω), the $\sqrt{-1}$ (j), the dielectric dispersion constant (B), and constant (n) [8].

CHAPTER 3: EXPERIMENTAL PROCEDURES

3.1 Zirconium Alloy Samples

The composition of pure zirconium (Goodfellow), Zry-4, and Zr-2.65Nb can be seen below in Table 1. Pure zirconium samples were cut from a rod with a SiC blade into discs (16mm x 2mm), while the Zry-4 and Zry-2.65Nb were cut into squares from thin plates (15mm x 15mm x 1.7mm). The samples were then polished at 600, 800, and 1200 grit, cleaned with acetone and DI-water, and then air dried. Samples were EIS tested in the pre/post breakaways oxidation conditions, as well as with no pre-treatment.

Table 2   Zirconium alloy compositions.

	Sn	Fe	Cr	H	Hf	N	O	Nb
Zr (ppm)	-	200	200	10	2500	100	1000	-
Zry-4 (wt. %)	1.2-1.7	0.18-0.24	0.07-0.13	-	-	-	0.1-0.14	-
Zry-2.65Nb (wt. %)	-	0.061	-	-	-	-	0.106	2.62
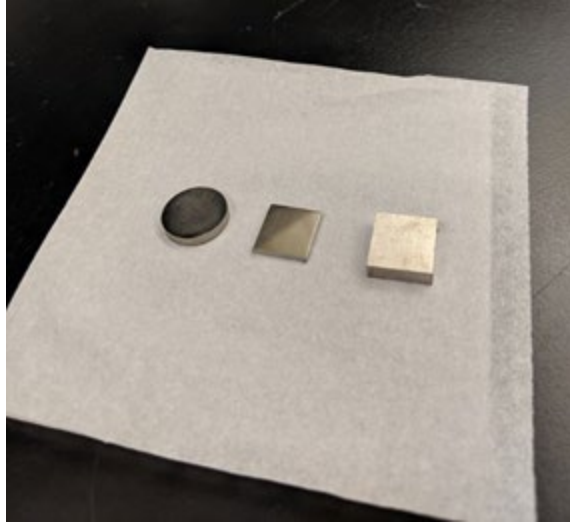
Figure 2   **Image of zirconium samples prior to room temperature EIS testing. On the left is the pure zirconium specimen, middle Zry-4, and right Zry-2.65Nb.**

3.2 Oxidation of Zirconium Samples

Samples were isothermally oxidized in dry air ($N_2 + 20\%O_2$) at 700°C in a NETZSCH STA-449 F3 Jupiter machine. Four samples of each alloy type were selected for oxidation, for various times in order to characterize pre- and post- breakaway oxide states. The isothermal oxidation times for each composition were pre-determined from a previous work that characterized the evolution of oxide formation on these zirconium alloys [43]. Below, in Figures 3-5, images before and after progressive oxidation pretreatments can be seen, as well as the generated mass gain curves during oxidation curves. For each alloy, each of the four samples was oxidized for a progressively longer duration and referred to by their oxidation state, OS1 to OS4, throughout this work.
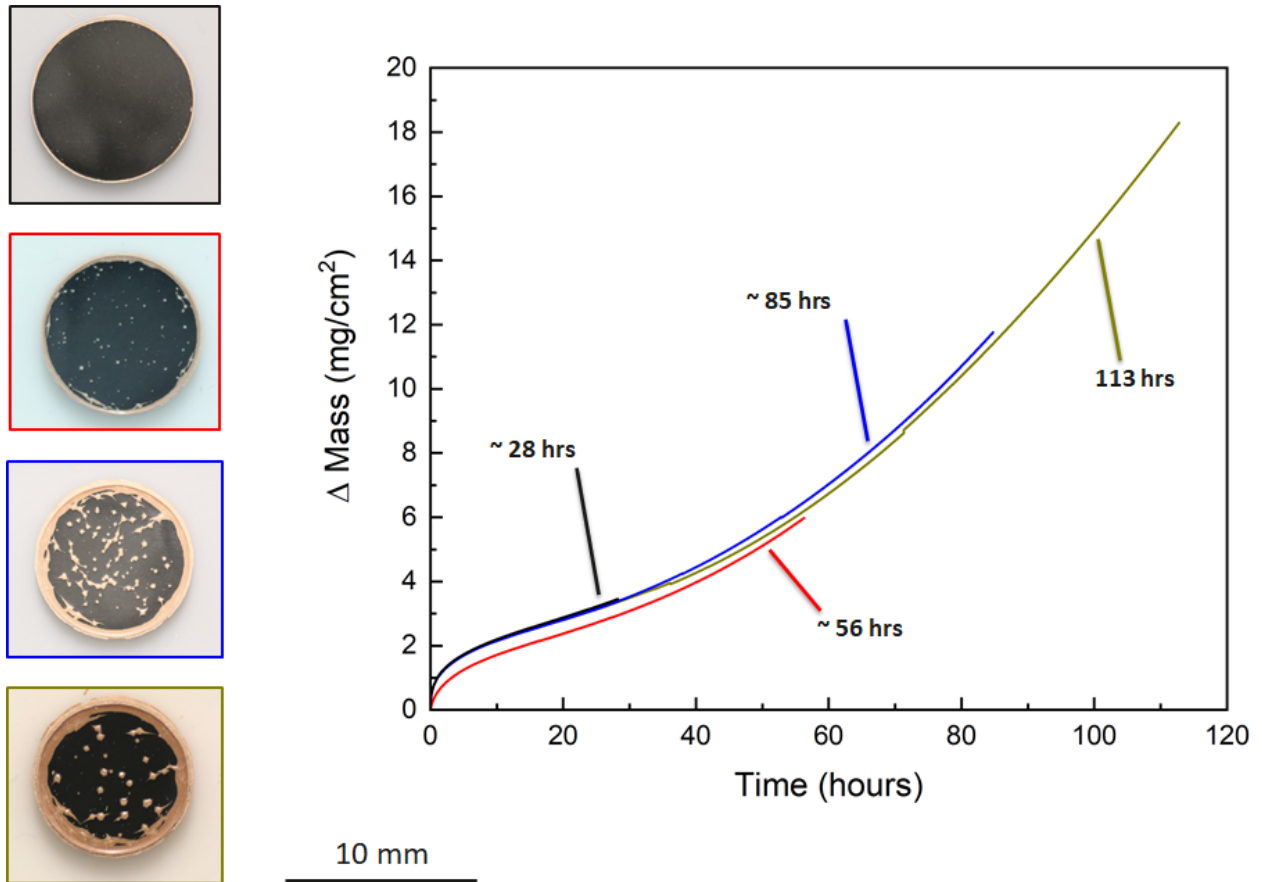
Figure 3   **Macro images of pure zirconium samples, before and after oxidation, with associated mass gain curves for processing.**
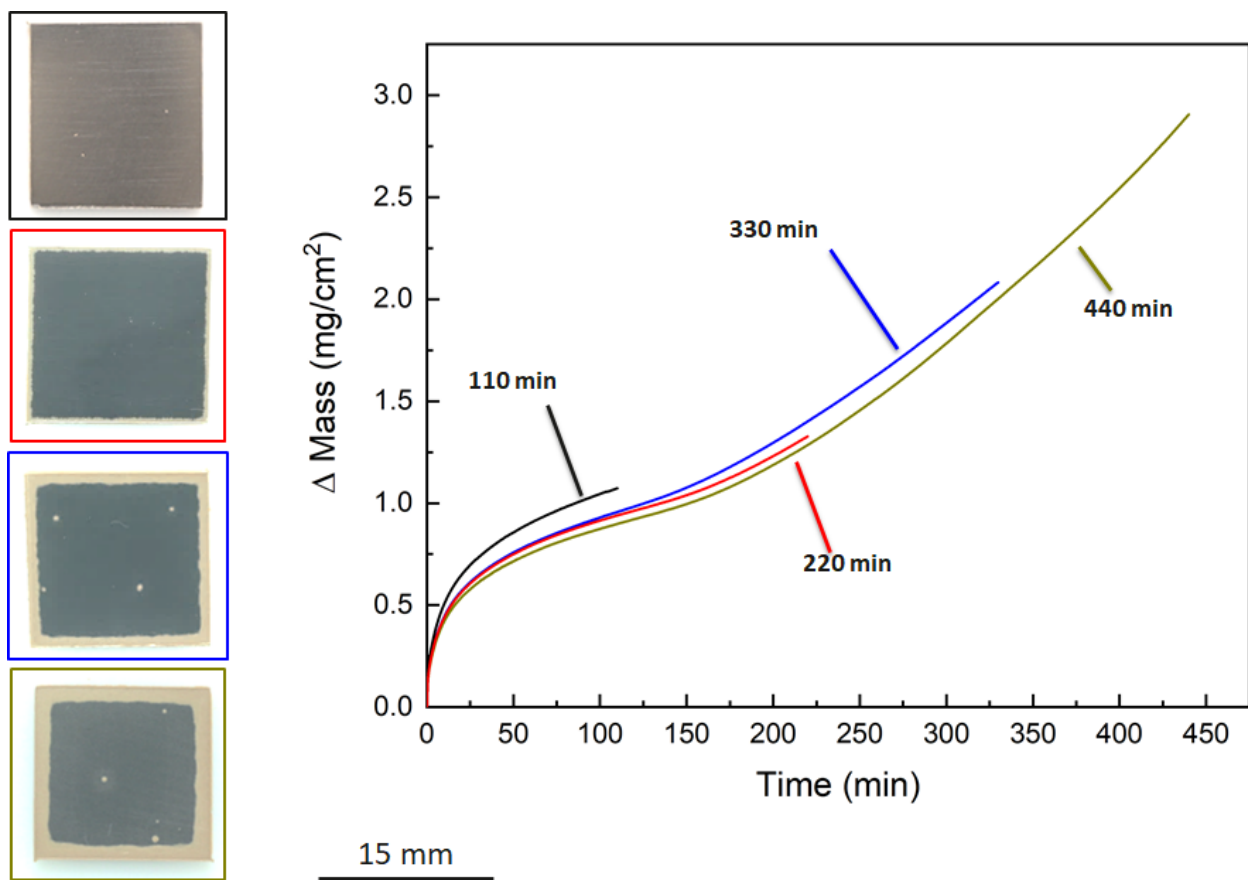
Figure 4   **Macro images of Zry-4 samples, before and after oxidation, with associated mass gain curves for processing.**
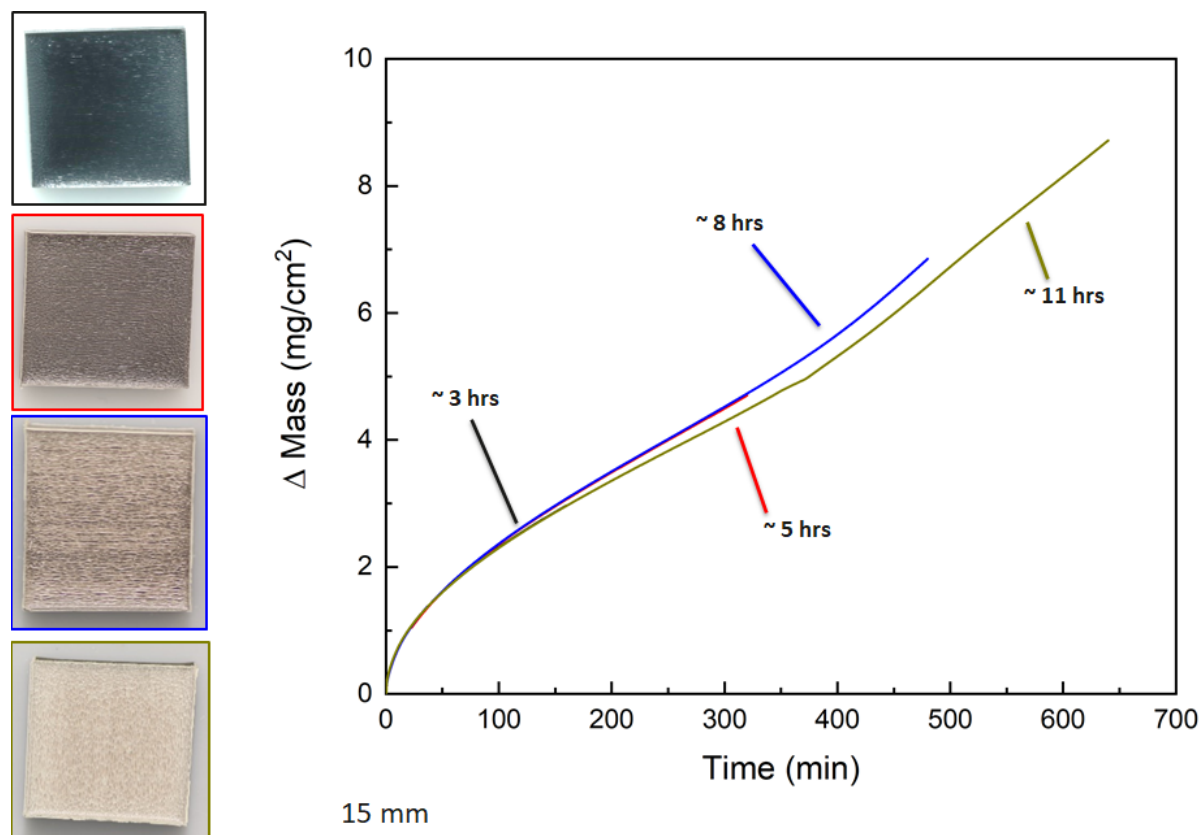
Figure 5 **Macro images of Zry-2.65Nb samples, before and after oxidation, with associated mass gain curves for processing.**

3.3 Room Temperature EIS Tests

The electrolytes chosen for this study were selected in order to simulate operating conditions found in that of a LWR in the field. Several previous studies [5, 15, 16, 18, 25, 39] performed EIS tests at these nominal LWR conditions, where temperatures reside around the 300°C -360°C mark, and LiOH and KOH water chemistries are approx. at the 2.2 ppm and 11ppm level, respectively. For this study, deionized water, 2.2 ppm LiOH (Fisher Scientific), and 11ppm KOH, served as the mediums for EIS testing. Samples were EIS tested in the pre/post breakaways oxidation conditions, as well as in the unoxidized state. Electrochemical impedance spectroscopy was performed with a Biologic SP-300 potentiostat, through a frequency range of .001 Hz – 6.000 MHz with an

amplitude of 10 mV, in a three-electrode glass cell (approx. 300 ml, seen below in Figure 6), with a platinum mesh counter electrode and saturated calomel reference (SCE) electrode. For each test, the open circuit potential (OCP) was monitored for approx. 2 hours, followed by the EIS scan, and then an additional OCP. This process was repeated an additional 3 times, resulting in 4 generated EIS curves per test, to instill confidence in results. The curve with the median most amount of electrolyte exposure time (Curve number two for each sample) was then selected for further evaluation and analysis. These curves were the impedance results selected for equivalent circuit modeling and were then used to identify trends and to help describe the physical processes occurring within the system. For all room temperature testing, the exposed sample area was 1 cm^2 for all samples.

Figure 6   Experimental setup for room temperature EIS testing.

3.4 Hydrothermal Reactor EIS Tests

Additional tests were performed at higher temperatures and pressures in a custom designed Parr Instruments 4760 Hydrothermal Reactor to simulate a near LWR environment. The reactor itself consisted of a T316 stainless steel vessel (300ml in volume), with a 2.5" ID and a 4" inside depth, and an electrical feedthrough from Conax at the vessel head which allowed two platinum 24G wires of 3.5" of length to enter the working zone. The vessel head was additionally equipped with a J-Type thermocouple, a 3000psi rated pressure gauge, a safety rupture disc set at approximately 2800psi, and a flexible graphite gasket to help seal the vessel during use. A cylindrical heater assembly was used for heating (115V, 800W) that coaxially slid around the vessel during testing. Temperature was controlled using a Parr 4848 Controller, visualized in Figure 7. In order to maintain the appropriate seal for testing, each of the six bolts at the vessel head were tightened to 35-ft-lbs with a torque wrench, in a criss cross pattern for uniform tightening. This tightening occurred after the compression ring on the two clamps were secured into place using an allen wrench tool. Pictures of the reactor assembled and testing can be seen below in Figure 8.

Figure 7   Reactor controller used in hydrothermal reactor tests.

Figure 8   **Hydrothermal reactor connected to potentiostat for impedance data acquisition (left) and before testing (right).**

For the experimental setup for the EIS portion of the experiment, a two-electrode system was utilized, with the working electrode being a cylindrical Zry-4 specimen with similar geometry to that of fuel cladding (1" long, ⅝" OD, 1mm wall thickness), and a pseudo-reference/counter electrode platinum mesh that coaxially surround the cylindrical zirconium specimen. The working distance between the two electrodes was approximately ⅜", with the excess platinum mesh being "crimped" at the top and the bottom to help hold the fixture together. Two alumina ceramic discs (Goodfellow, 1" OD, ⅜" ID, .0768" thickness) were used as a buffer material to prevent direct contact between the two electrodes. TIG welding was performed on the inside of the cylinders to attach it to a zirconium wire, which was then mechanically attached to the platinum wire coming into the vessel from the electrical feedthrough. The vessel itself was filled with 175ml of

electrolyte, consisting of 2.2ppm LiOH and 18.2 MΩ of millipore water for the Zr22

sample, to simulate in-core water chemistries. For the Zr23 specimen, 2.2ppm LiOH and

DI-water was used. The same EIS parameters used in the room temperature testing were

used for the hydrothermal reactor tests, with the exception of the number of cycles

performed.

Two Zry-4 cylinders were tested in this environment, with the first specimen

(Denoted Zr22) having 31 EIS scans performed over a period of three days, at a

temperature of 330°C at 1875psi. The second Zry-4 specimen (Zr23) was cycled a total

of 62 times (two tests performed back to back). The total test time for Zr22 was

approximately 64 hours, while Zr23 totaled out at approximately 139 hours (almost 6

days) of exposure time. Prior to EIS testing, a heat affected zone (HAZ) was observed on

these two cylinders after the TIG welding step (Figure 9). In order to evaluate whether

this had an effect on the resultant impedance, the Zr22 sample was not polished and EIS

tested as-received, and Zr23 was polished on the outer edge of the cylinder with 120 grit

sanding paper to attempt to remove this zone (Figure 10).
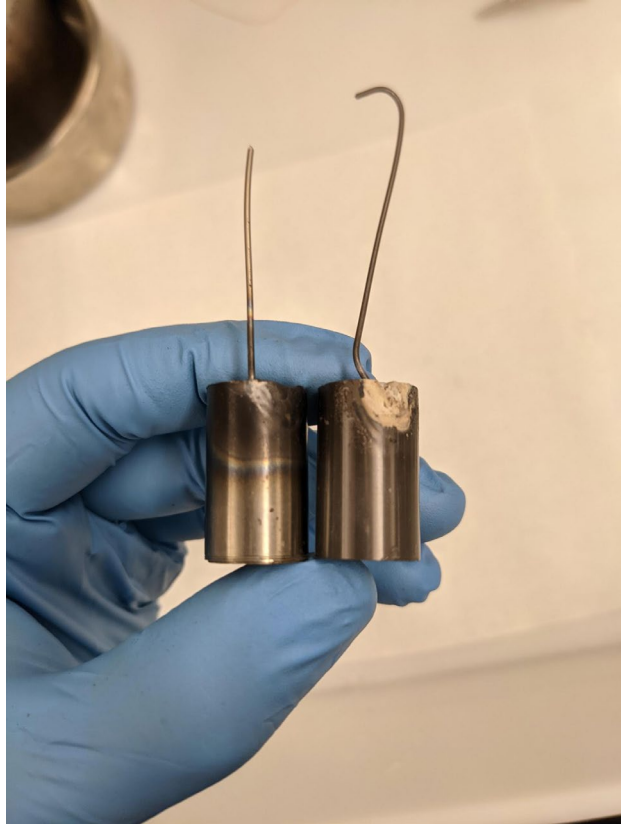
Figure 9   Zr22 (right, post high temperature run) and Zr23 (left, prior to EIS testing and surface polishing) HAZs from TIG welding process.

Figure 10   Zr23 surface polished prior to high temperature EIS run.

To ensure no overshooting occurred during the heating of the vessel, a

conservative ramp rate was utilized. The heater was raised to 200°C at the H1 power

setting (50% power), then increased to H2 (100% power) 25 degree/hr until 330°C was

reached. Thirty minutes were allowed to pass once temperature was obtained before

impedance data was taken, in order to ensure the electrodes had also reached temperature

and the system had stabilized. The testing environment in the vessel was static and was

not agitated. Figure 11 reveals the high-temperature EIS configuration completely

assembled.
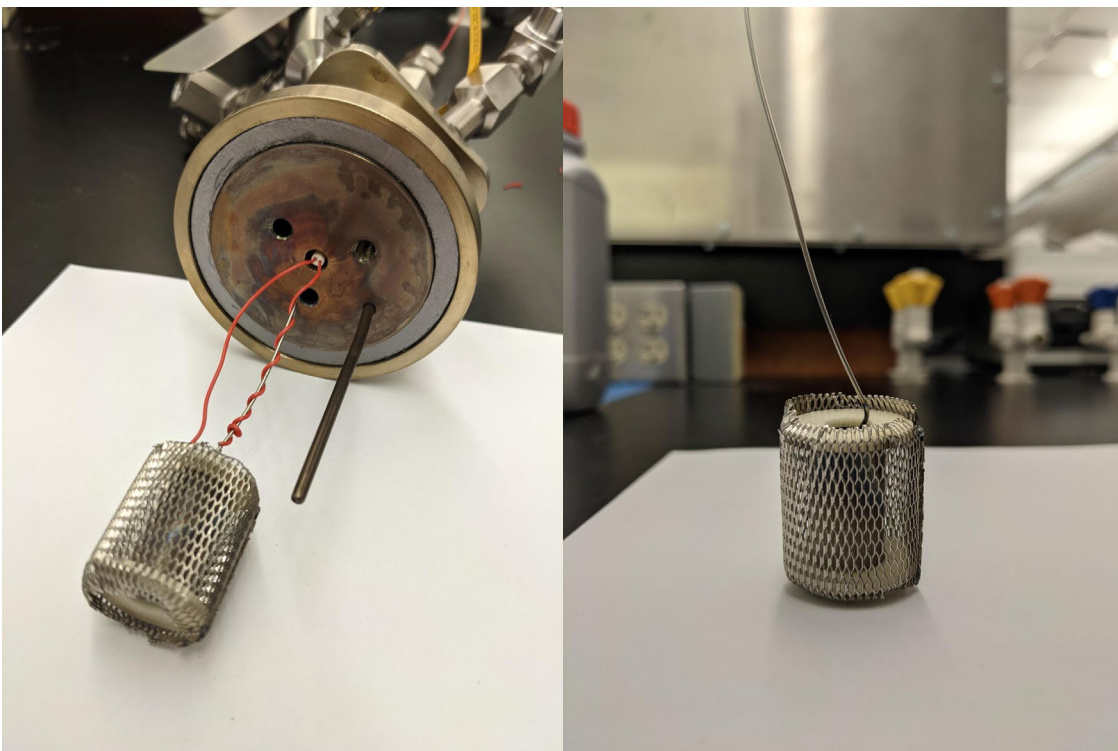
Figure 11   EIS configuration with electrical connections made (left) and prior to being added to the system (right). In the left image, the J-type thermocouple and flexible graphite seal can additionally be seen.

A small portion of the Zry-4 cylinder remained after chopping Zr22 and Zr23 to 1" segments, and was originally planned to undergo similar testing, with altered geometric conditions. However, after TIG welding the sample, it was determined that performing SEM/EDS analysis on the specimen to obtain before/after images would be of more utility for the sample. This sample was denoted as Zr24, and these images can be seen in the results section. Below in Figure 12, Zr24 is imaged.

Figure 12   Zr24 (right) after TIG welding process.

CHAPTER 4: RESULTS AND DISCUSSION

4.1 Oxide Thicknesses Derived via FESEM Analysis

Pure zirconium, Zry-4, and Zry-2.65 Nb samples were cross sectioned and polished up to 1 μm slurry after electrochemical testing in order to report the oxide thickness present via SEM analysis. A FEI Teneo Field Emission Scanning Electron Microscope (FESEM) was used to acquire these images. Special attention was paid to reduce charge build up during imaging, as to not distort the resultant images. Copper tape was used to ground the samples to the stage, as well as a carbon coating step to reduce charge build up on the sample. In order to determine the most representative oxide thickness of the tested samples, an average thickness was calculated by taking 5 thickness readings around the cross section of each sample. Below, in Figure 13, a snapshot from the NAV Cam view is shown, expressing where the thicknesses were observed and recorded to determine the average thickness.
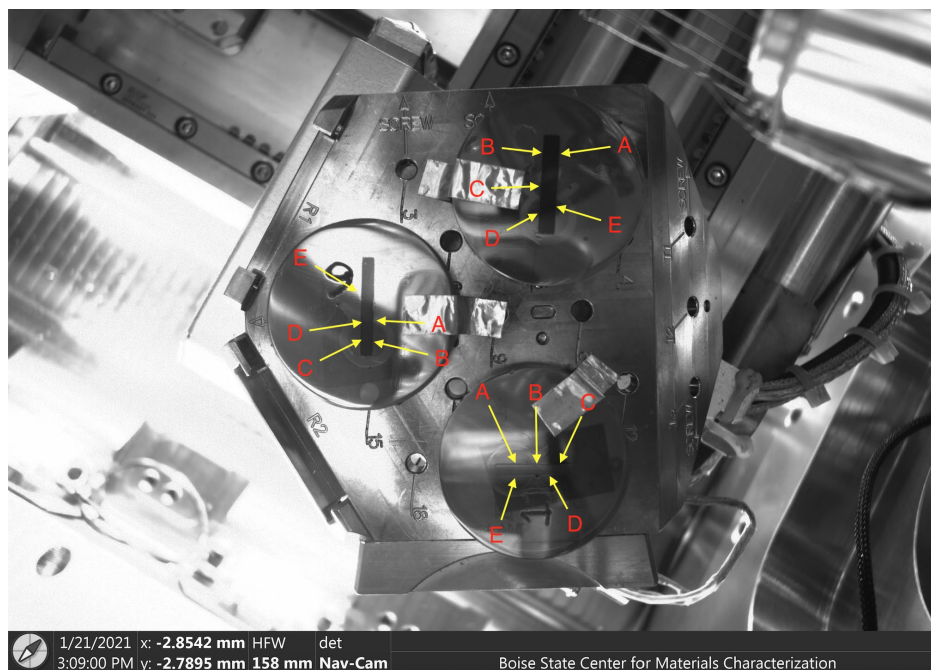
Figure 13 **NAV cam photo showing selected areas for average oxide thickness calculations.**

Table 3 shows the observed oxide thickness measurements for each oxidation state, and alloy of zirconium, as well as the standard deviations. For each environmental condition, the general trend is an overall increase in oxide thickness as the oxidation state progresses. In some instances, particularly for oxidation state four for each alloy, the measured accuracy of the observed thickness is approximate, as cracking from the oxidation period leaves gaps within the oxide which are included in the measured results. The oxidation kinetics for each alloy varies depending on the environment it is oxidized in. Considering each of these samples were oxidized in air, the observed thickness is what is to be expected for pure Zr, Zry-4, and Zr-2.65Nb.

Table 3   Average Oxide Thickness with increasing extent of oxidation (OS1-OS4) observed from FESEM imaging for Pure Zirconium, Zry-4, Zry-2.65Nb.

	Pure Zirconium				Zry-4				Zry-2.65Nb			
	OS1	OS2	OS3	OS4	OS1	OS2	OS3	OS4	OS1	OS2	OS3	OS4
Average thickness (μm)	13.66	22.13	22.73	100.67	6.61	9.48	10.90	16.55	21.38	24.20	39.03	48.31
Standard Deviation (μm)	2.89	14.65	5.25	73.57	1.09	3.38	5.20	9.16	5.26	4.69	8.98	11.16

<u>4.1.1 SEM Images for each alloy</u>

<u>Pure Zirconium</u>

Below in Figure 14, SEM images for pure zirconium reveal the progression of oxide growth. The oxide maintained a fairly compact structure throughout the majority of its development, with horizontal cracking becoming apparent at its 113-hour oxidation mark. The thicknesses recorded for this advanced stage of oxidation yielded can be seen in Figure 14d. The oxygen enriched zone can also be observed directly below the O/M interface for each OS, containing a thickness of roughly 3 microns.
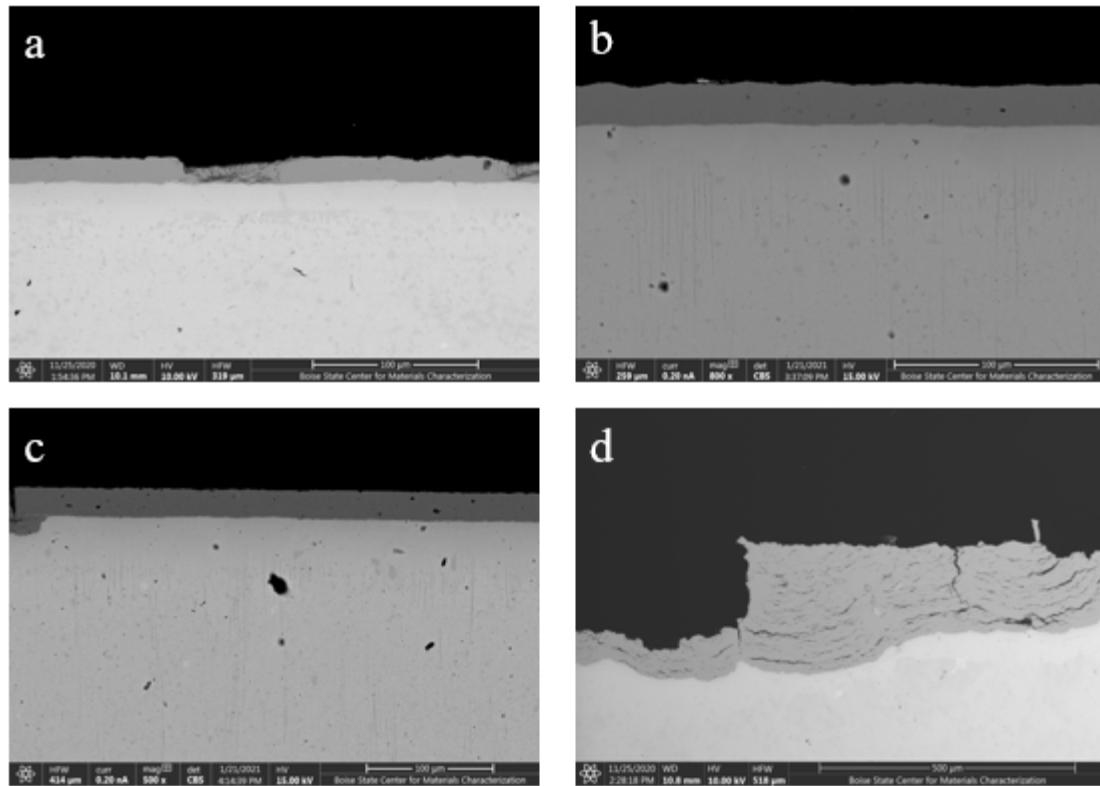
Figure 14   FESEM images for pure zirconium showing evolution of oxide growth. Image a.) shows Pure Zr at OS1, with b-d showing OS2-4, respectively.

Zry-4

Some delamination can be observed at the O/M interface for OS2 for the Zry-4 sample, presented in Fig 15b. This is the result of the initial stage of the oxide breakaway phenomenon. Additionally, a darker gap can be seen at the epoxy/oxide interface, most likely due to epoxy shrinkage during curing. Lateral cracking is obvious in Figure 15d, expected of that of post breakaway samples. The oxide itself contains a wavy, undulating configuration at the O/M interface, primarily observed for the Zry-4 and Zry-2.65Nb samples. Similar to the pure zirconium samples, an oxygen enriched zone can be observed below the O/M interface of interest for Zry-4, as well as Zry-2.65Nb samples. Some initial lateral cracking is also present at the OS-3 (15c) oxide layer.
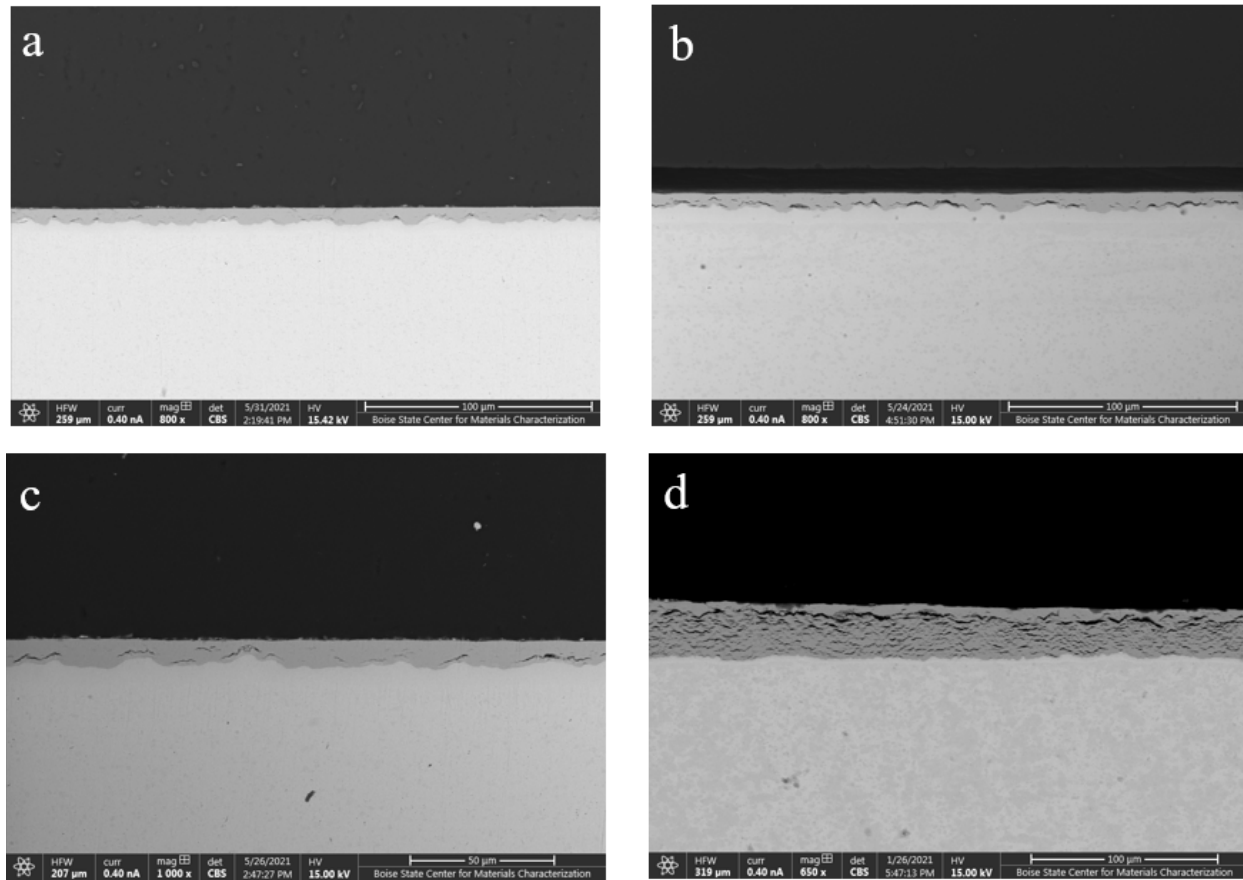
Figure 15   FESEM images for Zry-4 showing evolution of oxide growth. Image a shows Zry-4 at OS1, with b-d showing OS2-4, respectively.

<u>Zry-2.65Nb</u>

The Zry-2.65Nb samples exhibited lateral cracking along the oxide in Figure 16, with a more exaggerated amount of cracking present towards the later oxidation states. This alloy of zirconium appears to have experienced a certain degree of "curling "or "spalling", with additional breaks in the oxide forming from residual stresses formed in the layer. Due to this oxide degradation behavior, accurately recording the oxide thickness via SEM analysis proved to be challenging. Measurements for thickness were

recorded towards the middle of spalling points, in order to effectively not account for lengths of oxide at each end of the curl.
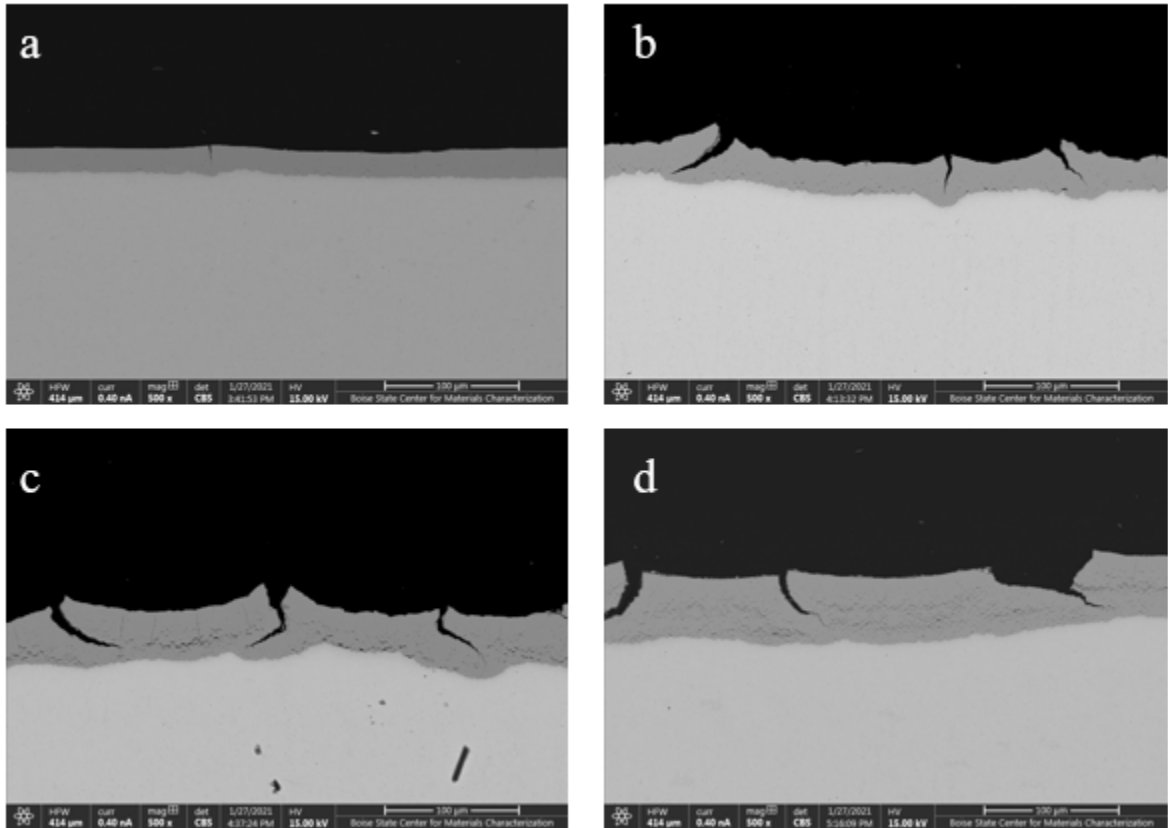
Figure 16   FESEM images for Zry-2.65Nb showing evolution of oxide growth. Image a.) shows Zry-2.65Nb at OS1, with b-d showing OS2-4, respectively.

Zry-4 High Temperature Sample, (Zr22)

Below in Figure 17, a close up image of the oxide formed on the Zry-4 cylinder tested at 330°C can be seen. The oxide, approximately 1-2 microns in thickness, appears to be intact and in good condition, as expected for the fuel cladding alloy. A small dip can be observed at the epoxy/oxide interface, due to epoxy shrinkage after the curing phase. The metal/oxide interface appears to have an undulating structure, along the

meshing of the two areas. This oxide presented at 330°C yields a formed structure

expected of these conditions, and represents the protective barrier used in LWRs.
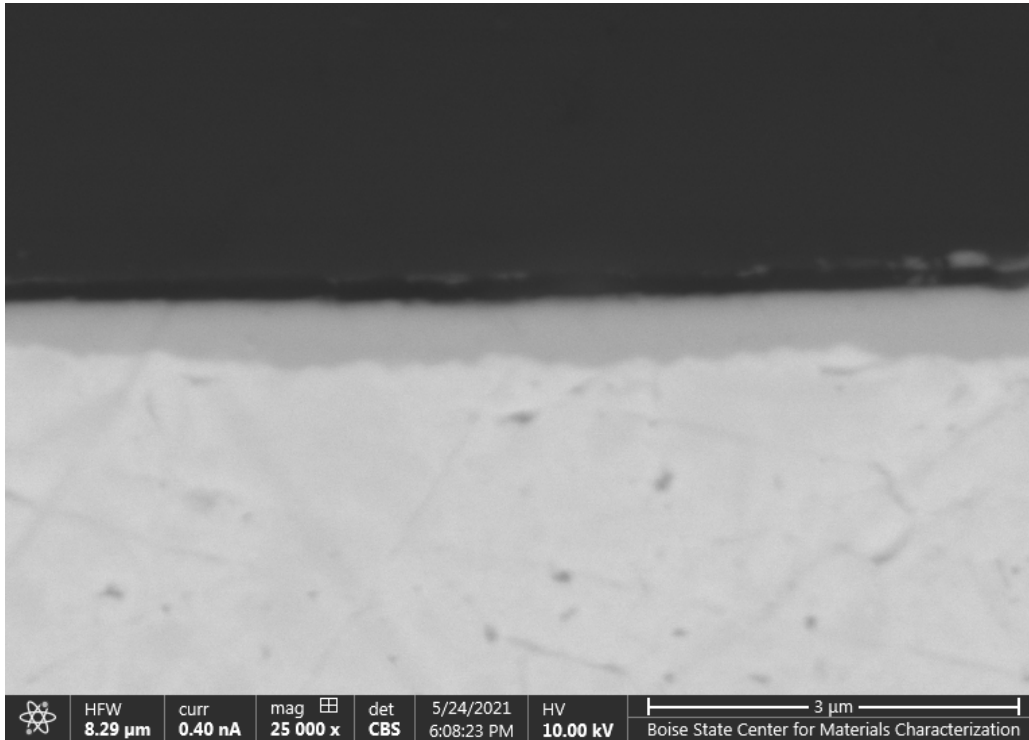
Figure 17   **FESEM images for Zr22 (Cylindrical Zry-4 specimen) showing developed, intact oxide after high temperature exposure.**

Zry-4 High Temperature (Zr23)

The Zr23 specimen pictured below in Figure 18 (also tested at 330°C at 1875psi, 138-hour exposure time), additionally yielded a compact, and dense oxide film after the EIS cycling. A similar undulating oxide/metal interface was observed as well as the thin epoxy gap as seen previously with the Zr22 sample. The observed oxide for Zr22 and Zr23, both in structure and in thickness, is in accordance with what is expected of the processing conditions from literature [14].

HFW	curr	mag ⊞	det	5/31/2021	HV	
8.29 µm	0.40 nA	25 000 x	CBS	2:28:45 PM	10.00 kV	Boise State Center for Materials Characterization
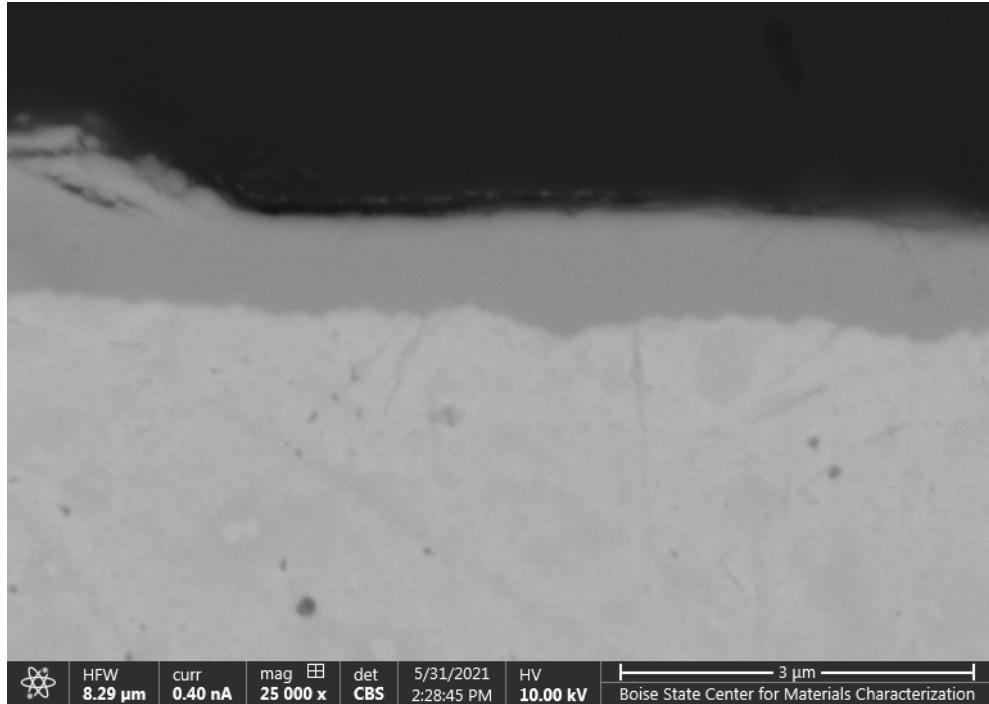
Figure 18   FESEM images for Zr23 (Cylindrical Zry-4 specimen) showing developed, intact oxide after high temperature exposure.

Zry-4 As-Received Specimen (Zr24)

The remaining segment from the original Zry-4 cylinder yielded a very thin (approx. > 1 micron thick) oxide film present on its surface. A similar wavy interface between the metal and the oxide was present, representative of the growth expected for that of a Zry-4 alloy. This SEM image was taken in order to observe what the fuel cladding surface resided in, prior to service in the elevated aqueous environment. The oxide itself appears to be intact, with no lateral or vertical cracking present, presented below in Figure 19.
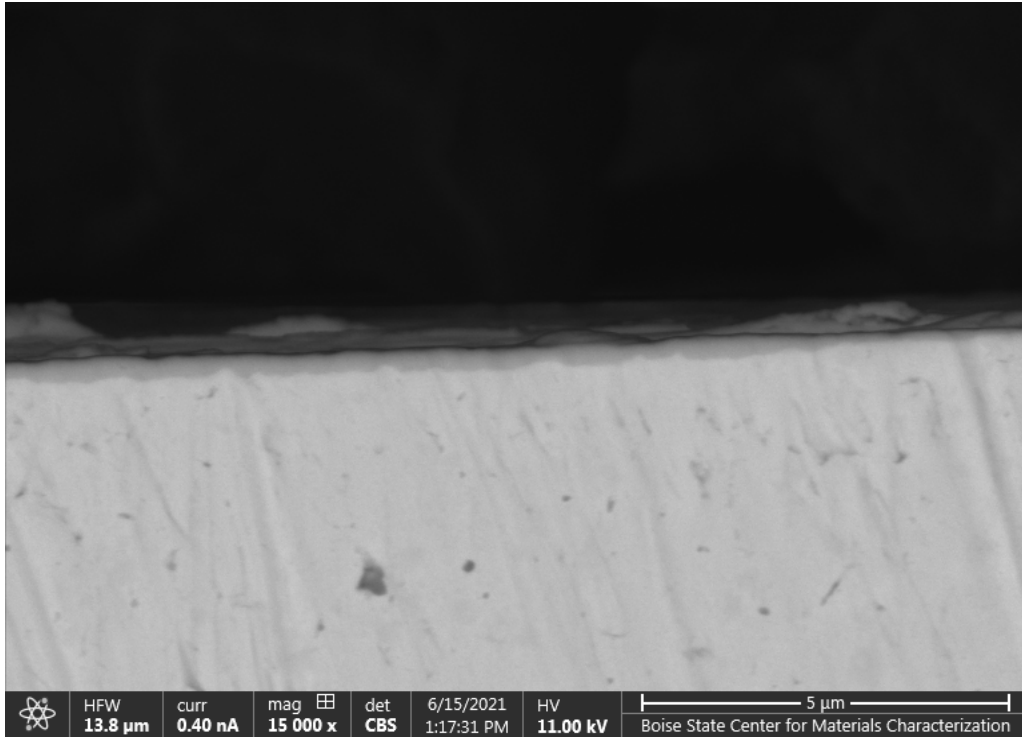
Figure 19   FESEM images for Zr24 (Cylindrical Zry-4 specimen) showing native, intact oxide.

4.1.2 EDS Analysis

Pure Zirconium

The EDS maps below reveal elemental compositions of the epoxy, oxide, and base zirconium metal for varying samples. Below in Figure 20, EDS mapping of OS-4 for pure zirconium can be seen. At the top portion of the SEM image, the epoxy is present, and EDS spectra identified larger amounts of C and O in this region. The oxide was cracked, non-uniform, and had the elements of Zr, Nb, and Cr, and Sn as identified by EDS analysis.

Electron Image 1

250µm

C Kα1_2

O Kα1

Cr Lα1,2

Zr Lα1

Nb Lα1

Sn Lα1
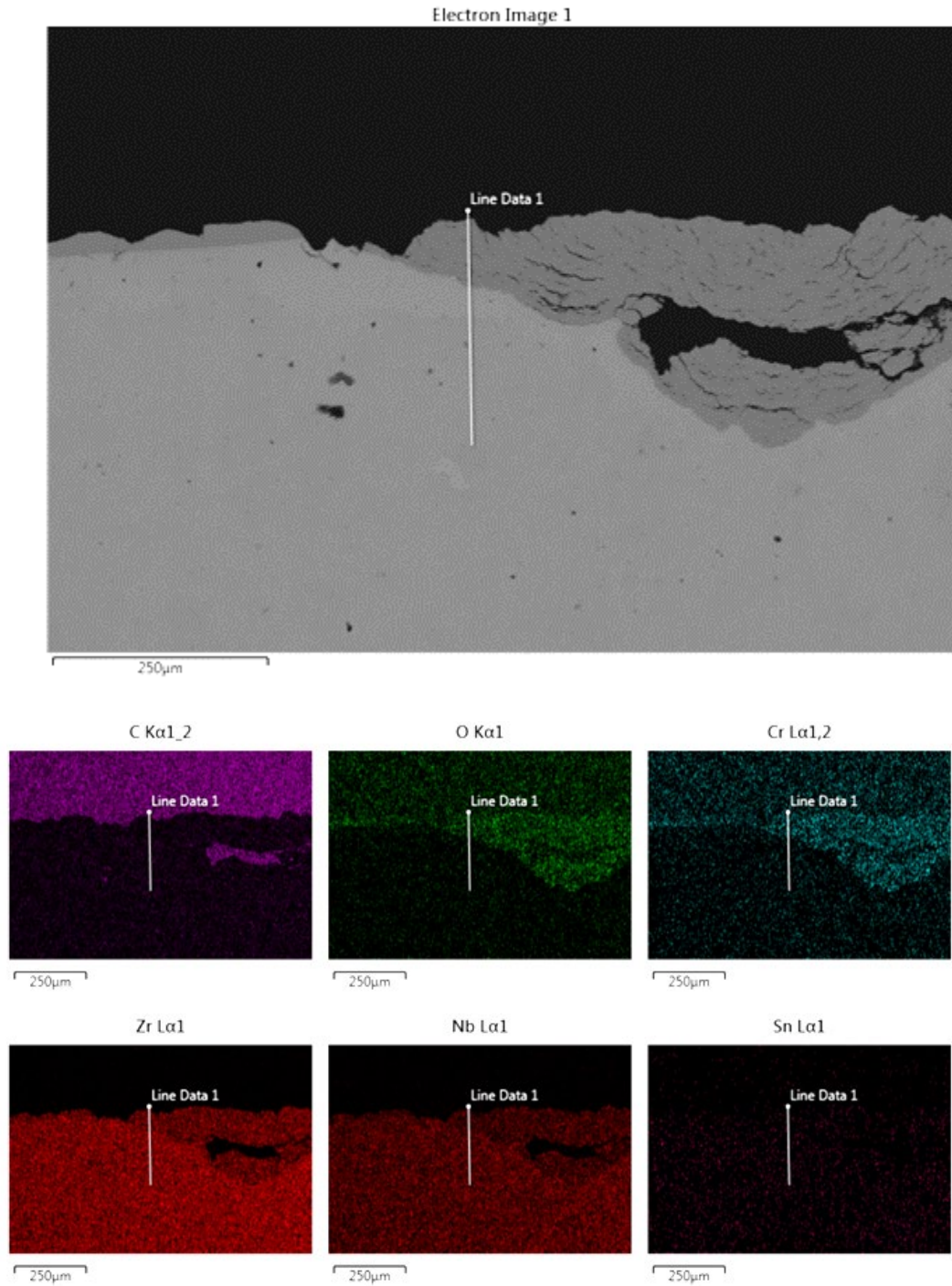
Figure 20   EDS spectra for OS4 for pure zirconium.

<u>Zry-4</u>

Some delamination can be seen in Figure 21 for OS-2 of the Zry-4 specimen,

most likely as a result of initial stages of breakaway oxidation following the development

of a wavy interface. The oxide layer itself is compact, with minimum to no horizontal cracking present. EDS spectra revealed enhanced levels of C and O in the epoxy, Zr, O, and Sn in the oxide layer, as well as in the bulk, with additional amounts of Cr found in the bulk. Limited, if any, counts of Fe were present in the mapping spectra. It is known that the oxidation of zirconium in air versus water yields different resultant oxide structures, and that the protective oxide barrier in aqueous solutions forms more favorably for Zry-4 and Zry-2.65Nb alloys. Since these two alloying variants were oxidized in air, the resultant oxide formed suffered in its structural integrity, compared to that if it had been processed in an aqueous environment.
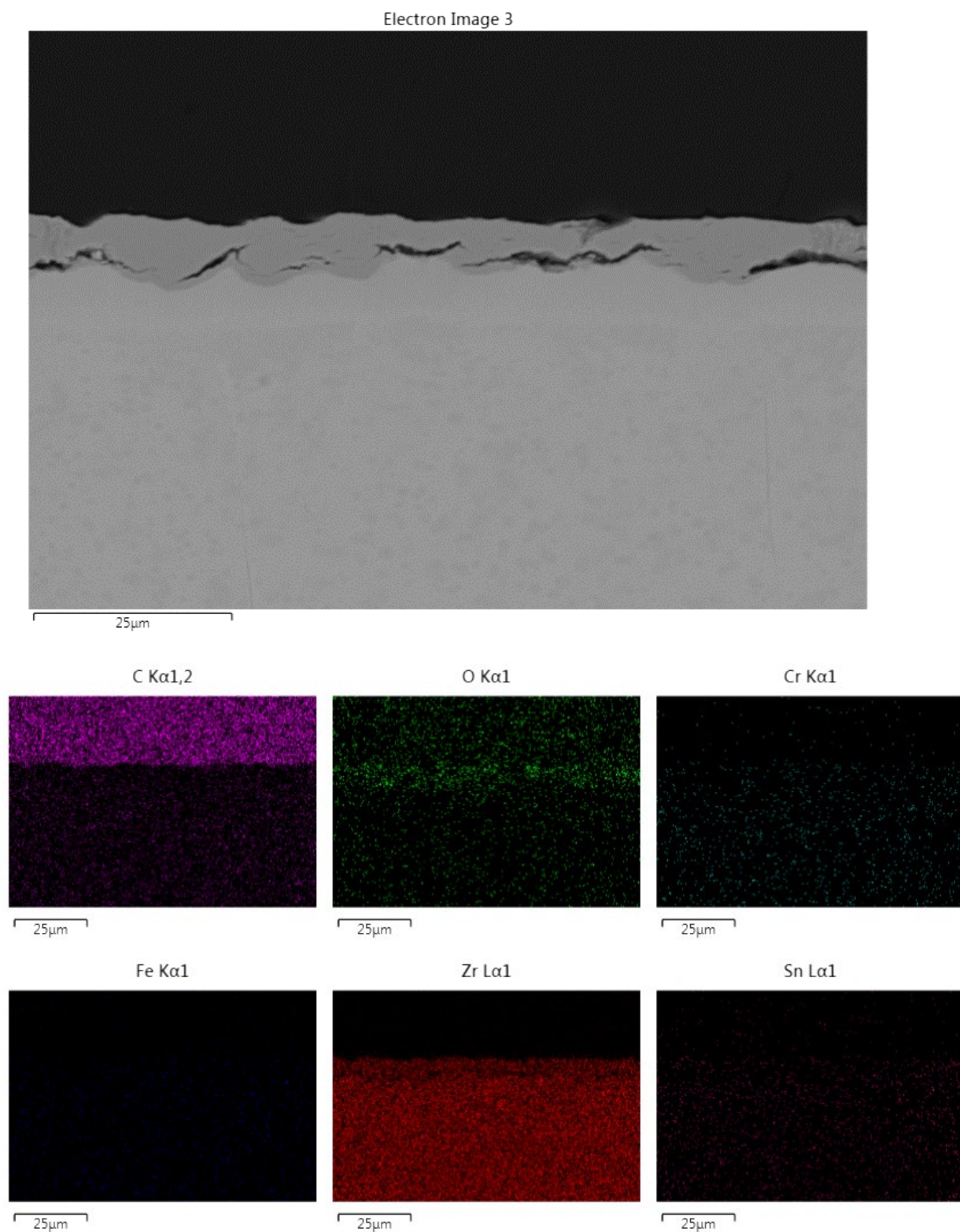
Figure 21   EDS spectra for OS2 for Zry-4.

Zry-2.65Nb

EDS spectra for OS-2 of the Zry-2.65Nb sample in Figure 22 follows the same identifying trends as the previous samples, with a noticeable presence of the Nb additional alloying element. A distortion or disturbance can be seen at the epoxy/oxide interface and is most likely an oxide spall crack that originated from the underlying O/M interface depression. The oxide layer is rich with Zr, O, and Nb, with some additional counts of Fe present in the bulk of the sample. Small lateral cracking can also be seen close to the metal/oxide interface.
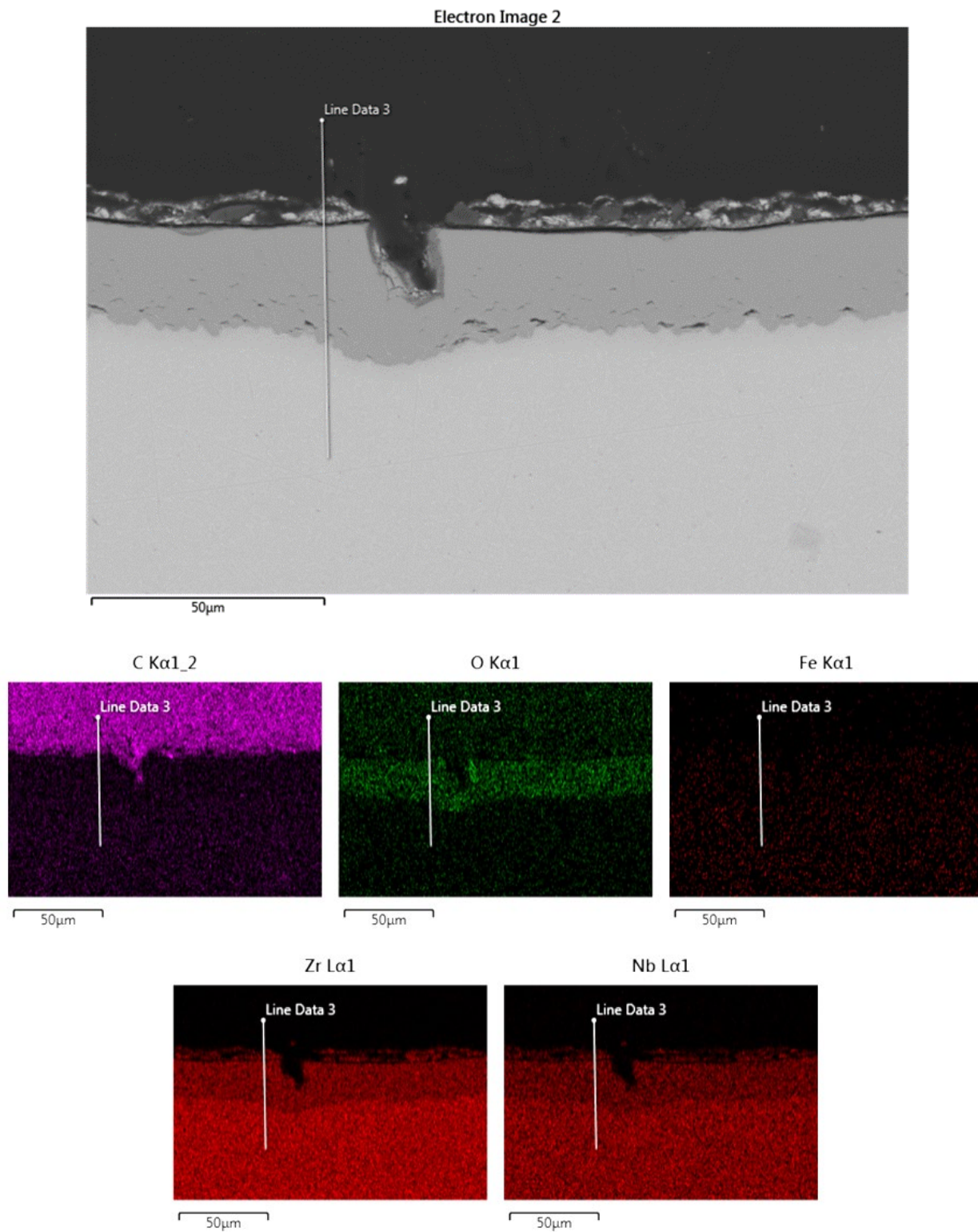
Figure 22 **EDS spectra for OS2 for Zry-2.65Nb.**

<u>Zry-4 High Temperature Runs</u>

The EDS analysis for the Zr22 in Figure 23 and Zr23 in Figure 24, respectively, reveal an elemental composition one would expect of Zry-4 alloy, in the pre-transition region. Both samples possess elevated levels of C and O in the epoxy region, with Cr, Fe, Zr, Sn present in the oxide and the bulk. Enhanced amounts of O are also present along the oxide/metal interface. No horizontal or resultant cracking was observed in either of these samples.

Electron Image 1

C Kα1,2

O Kα1

Cr Kα1

Fe Lα1,2

Zr Lα1

Sn Lα1
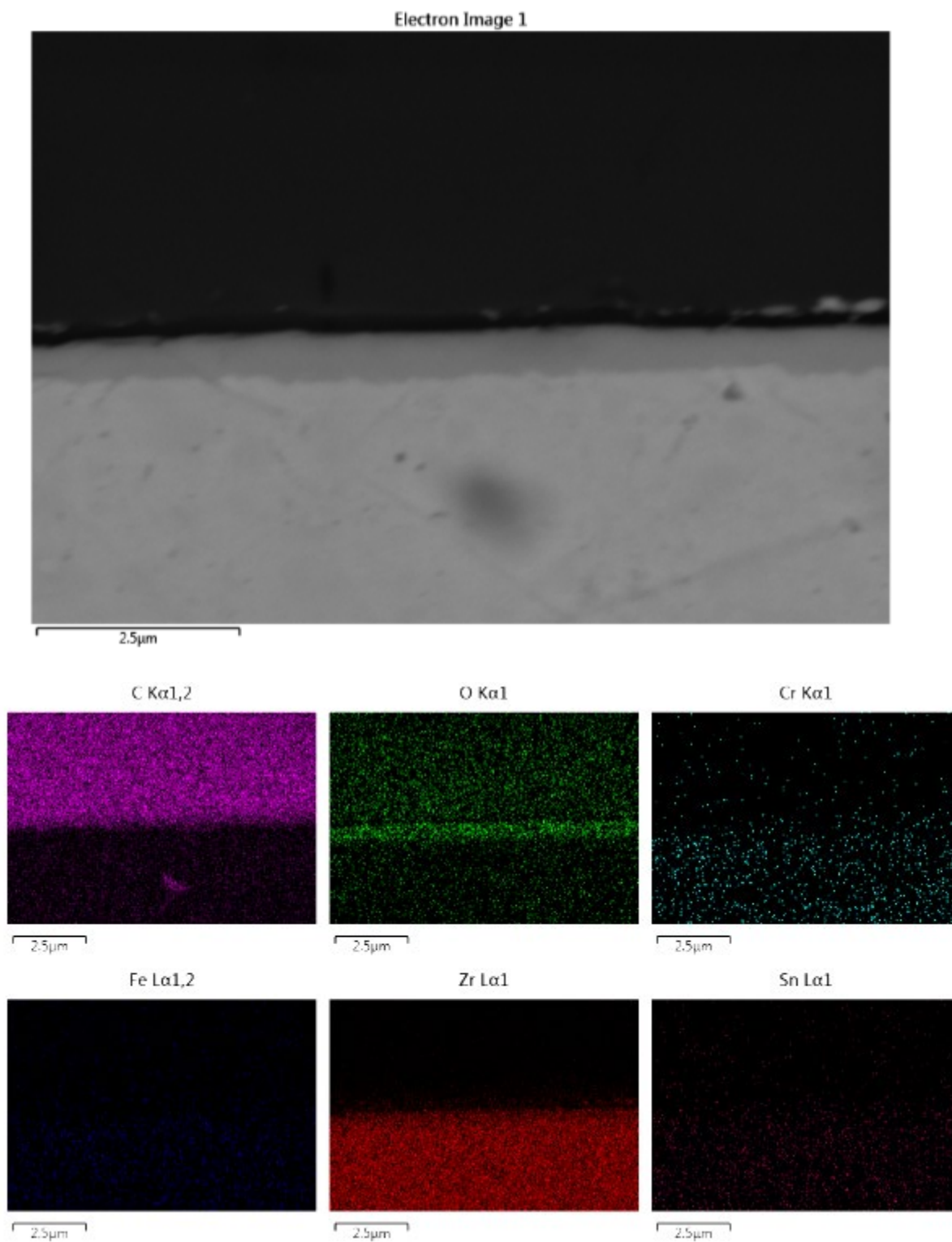
Figure 23   EDS spectra for Zr22.

Electron Image 5

2.5μm

C Kα1,2

O Kα1

Cr Kα1

100μm

100μm

100μm

Fe Kα1

Zr Lα1

Sn Lα1

100μm

100μm

100μm
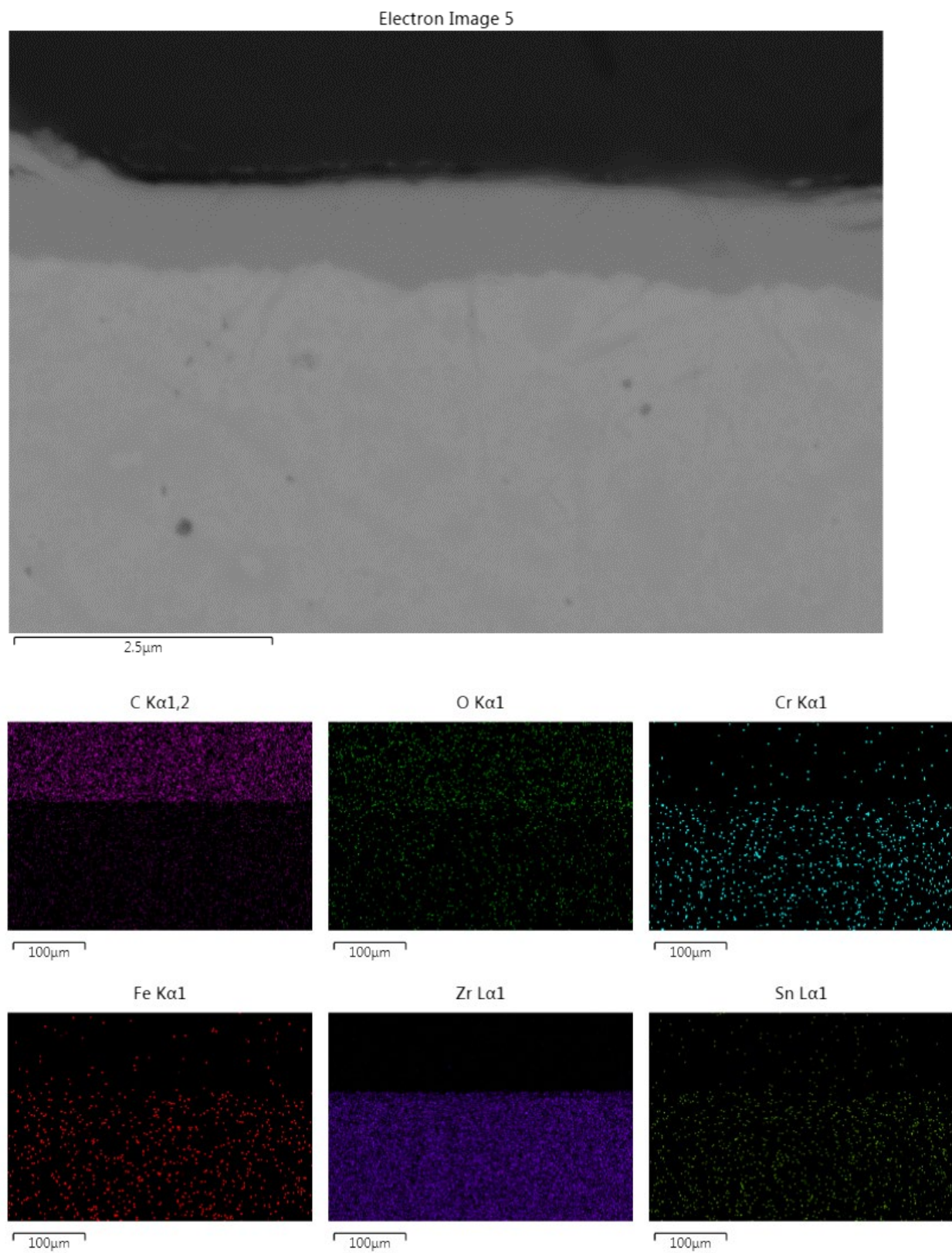
Figure 24   EDS spectra for Zr23.

The native oxide present on Zr24 in Figure 25 is so thin, accurate EDS spectra could not be resolved to identify the oxygen present. The remaining elements, however, continue to follow suit for those identified in Zr22 and Zr23, with Fe, Sn, Zr, and O located in the bulk, and elevated C amounts in the epoxy layer.

EDS Layered Image 1

C Kα1,2   O Kα1   Cr Kα1

Fe Lα1,2   Zr Lα1   Sn Lα1
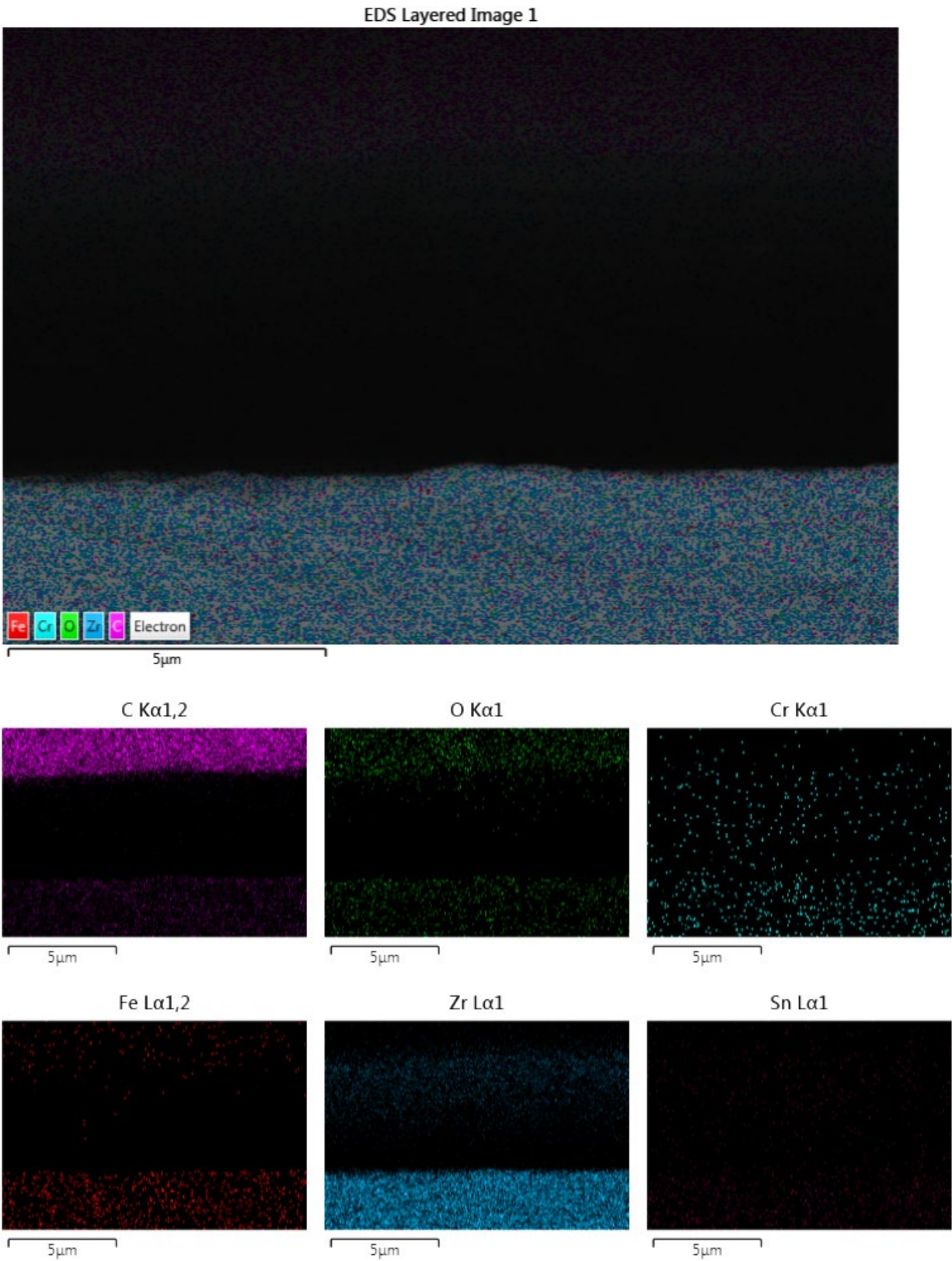
Figure 25   EDS spectra for Zr24.

4.2 Equivalent Circuit Modeling

To better understand the physical processes associated with the zirconium oxidation system, equivalent circuit modeling (ECM) was utilized to facilitate the EIS analysis. ECM serves as a benchmark method for dissecting EIS data by providing a platform to quantify reactions occurring at the oxide, and the interfaces between it, the electrolyte, and the bulk metal. The zirconium oxide system is an evolving one, with porous and dense layers becoming apparent as oxidation time increases. In order to accommodate this developing oxide, different ECMs are needed to best represent the current state of the oxide. At the initial oxidation period, a simple Re-Rc||Cdl circuit (Figure 26a) can be used. After this a dense layer can be observed closer to the metal/oxide interface, with a more porous structure located at the electrolyte/oxide interface. This circuit was found to be best represented by a Re-Rct||Cdl-Rct||Cdl circuit (Figure 26b). Towards the end of the oxidation process performed in the study, the addition of a constant phase element (CPE) was introduced, as the system at this point was not representative of an ideal capacitor. This alteration in the circuit was determined via literature review as a better way of representing the real-life conditions of the circuit [5, 7-11, 14, 15, 17, 19, 23, 27]. Below, in Figures 26c, the evolution of the ECMs used can be seen. For the fitting performed in this study, Circuit B was utilized for pre-transition samples, and Circuit C was used for post-transition samples.
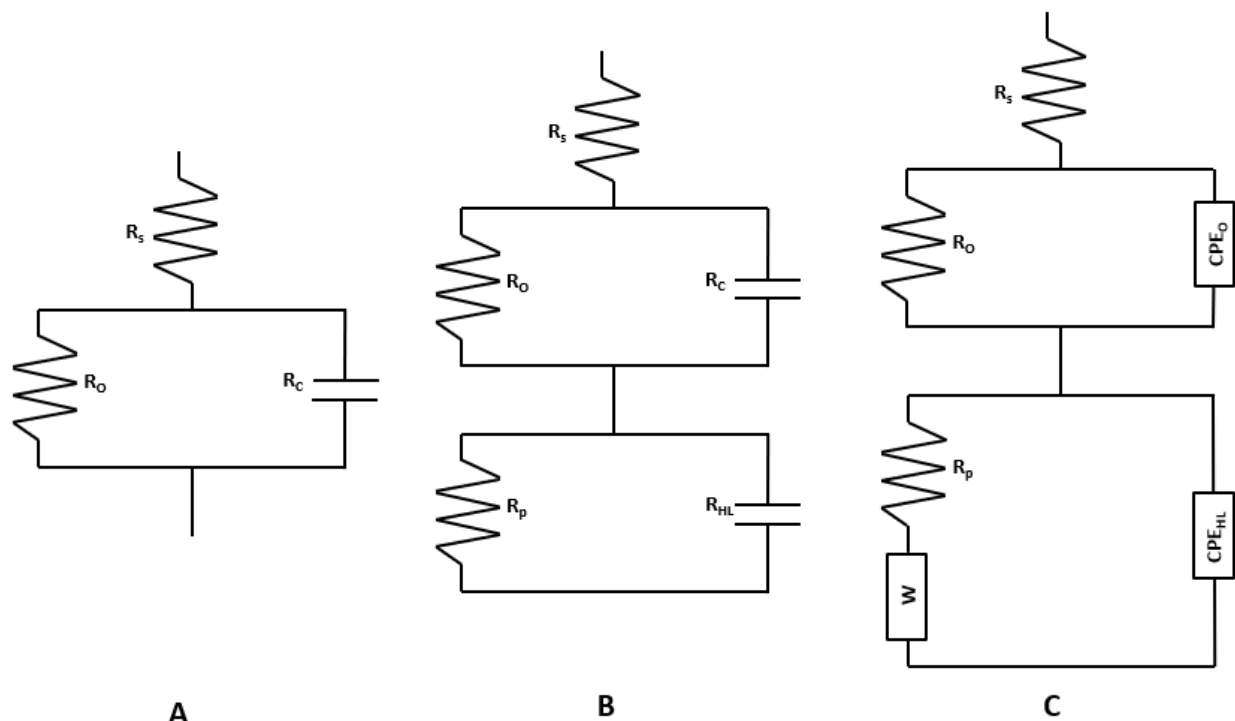
Figure 26 **Variations in equivalent circuits. Circuit (a) constitutes zirconium oxide before breakaway. It is represented by a basic oxide capacitor and resistor as well as a solution resistance. Circuit (b) shows zirconium oxide after break away, and includes an extra resistor and capacitor to represent a separate oxide phase. Circuit (c) is an evolution of circuit (b), in which the capacitors are replaced by one or more constant phase elements. Other factors are now included, such as polarization resistance, double layer (Helmholtz) capacitance, and Warburg impedance.**

4.2.1 Clarification of Selected Frequency Range for ECM

The frequency range observed for this study spanned from 10^{-5} to 10^6 Hz. However, for the fitted impedance graphs, a more specific frequency range (10^{-3} to 10^4), was selected. From literature, observed frequency ranges of impedance data typically varied from 10^{-6} to 10^6 Hz, more typically from 10^{-3} to 10^6 Hz [5, 7-11, 14, 17, 23, 25, 27]. Higher frequencies include parasitic noise from the wiring, potentiostat, and the environment can influence the produced curves, and make the analysis more difficult. In order to pull meaningful, consistent conclusions from the curves, the tighter frequency range was reported.

4.2.2 Impedance Fitting

In order to understand and pull meaningful information from impedance data, some estimations must be made about the zirconium oxide system and its structure. Once these assumptions are made, and an ECM selected, trends and observed behaviors of results can be determined to make conclusions about the physical processes occurring in the material system. By maintaining a close eye on alloying elements, exposed electrolytes, the oxidation state the oxide is in, and the resultant oxide thicknesses generated from oxidation, these conclusions can help lead to better designing decisions when using zirconium as nuclear fuel cladding for light water reactors.

4.3 Impedance Data for Oxidation Evolution

Evolution of zirconium oxides plays a paramount role in terms of oxide performance and impedance data interpretation. For the zirconium oxide system researched in this work, four different oxidation states were studied. The following is an overview of impedance spectra obtained from EIS testing on the pre-oxidized zirconium samples. Impedance results are presented primarily in Bode form, in the frequency range of 10^{-3} to 10^4 Hz. Nyquist plots are presented in the Appendix section. Electrochemical impedance spectra in Bode form are shown in the following sections, with the fitted data being the smooth line, and the experimental data points represented by textured lines. For the generated Bode plots, as oxidation state progresses from the pre- to the post-breakaway state, the impedance experiences an overall drop, from approx. 10^9 ohms to approx. 10^7 ohms. As the frequency increases, a general decrease of impedance can also be seen.

Below, in Figure 27, log (|Z|/Ohm) vs. oxidation time is presented at the frequency of 10.024 mHz for each alloy studied. Generally, as oxidation time progresses, for each alloy resultant impedance experiences a drop in value. For pure zirconium, OS1-3 represents an oxide that is still mostly intact and dense and yields an impedance similar in value to one another. Once breakaway occurs, a major drop of approximately 2 magnitudes of difference becomes apparent, at the 113-hour oxidation mark. The time taken to reach the post-transition region for pure zirconium takes much longer than that of the Zry-4 and Zry-2.65Nb samples, generating the need to present a superimposed graph of the two alloys log |Z| for clarity. OS1 for Zry-4 has an impedance value slightly higher than Zry-2.65Nb, however, both follow similar patterns to breakaway and yield a few magnitudes lower impedance at OS4. These alloys at their respective OS1 marks appear mainly intact, and compact. However, at the OS2-4 stages degradation appears to begin, and a decrease in the resultant impedance is apparent.
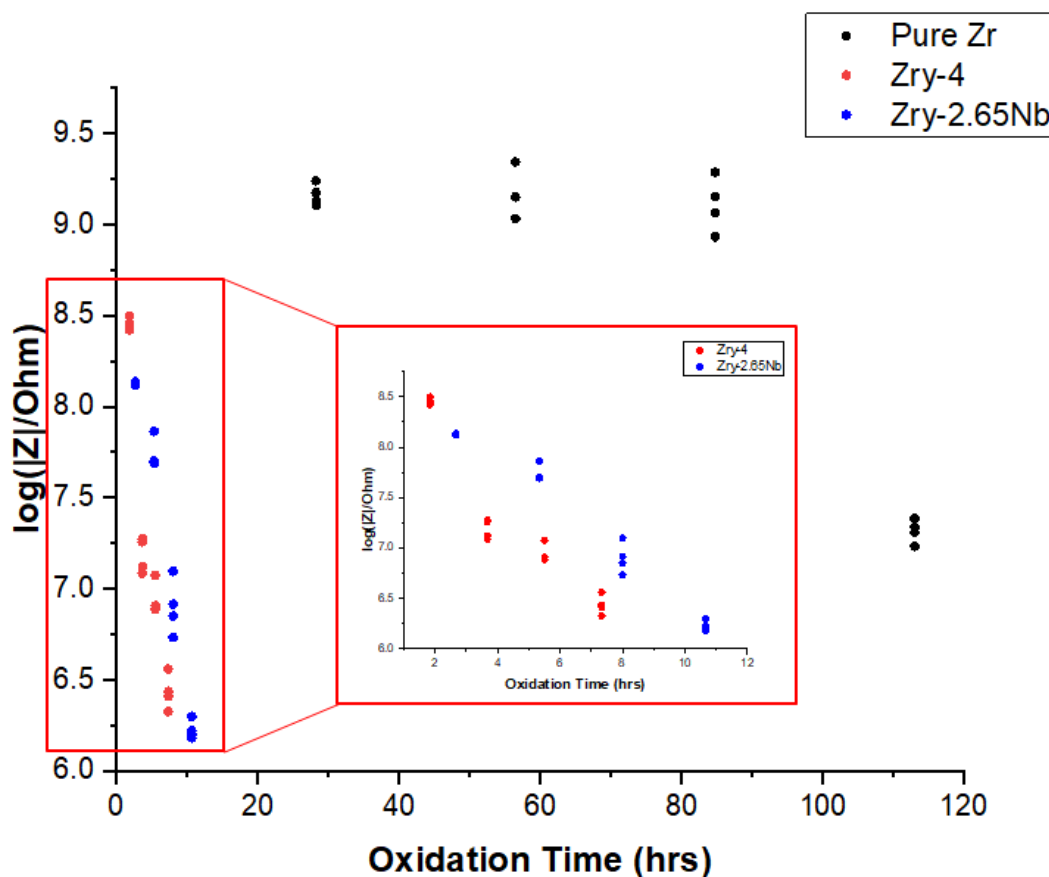
Figure 27 **Log(|Z|/Ohm) vs. oxidation time at 10.024 mHz for pure zirconium, Zry-4, Zry-2.65Nb.**

4.3.1 Impedance Measurement at a Single Oxidation State

Each EIS test was performed a total of four times to instill confidence in the generated results, and to allow the system to arrive at a steady state to retrieve data. Below in Figure 28, impedance data for OS1 of pure zirconium can be observed for each of the four cycles performed on it. Good repeatability was obtained for the duration of this test, with the exception of the low frequency Nyquist data (Located in the Appendix section), which is more erratic in nature due to the high resistance of the intact oxide

present on the sample. At the higher frequency ranges, the expected semi-circle of the Nyquist plot is apparent, with similar increasing impedance trends present for each cycle.
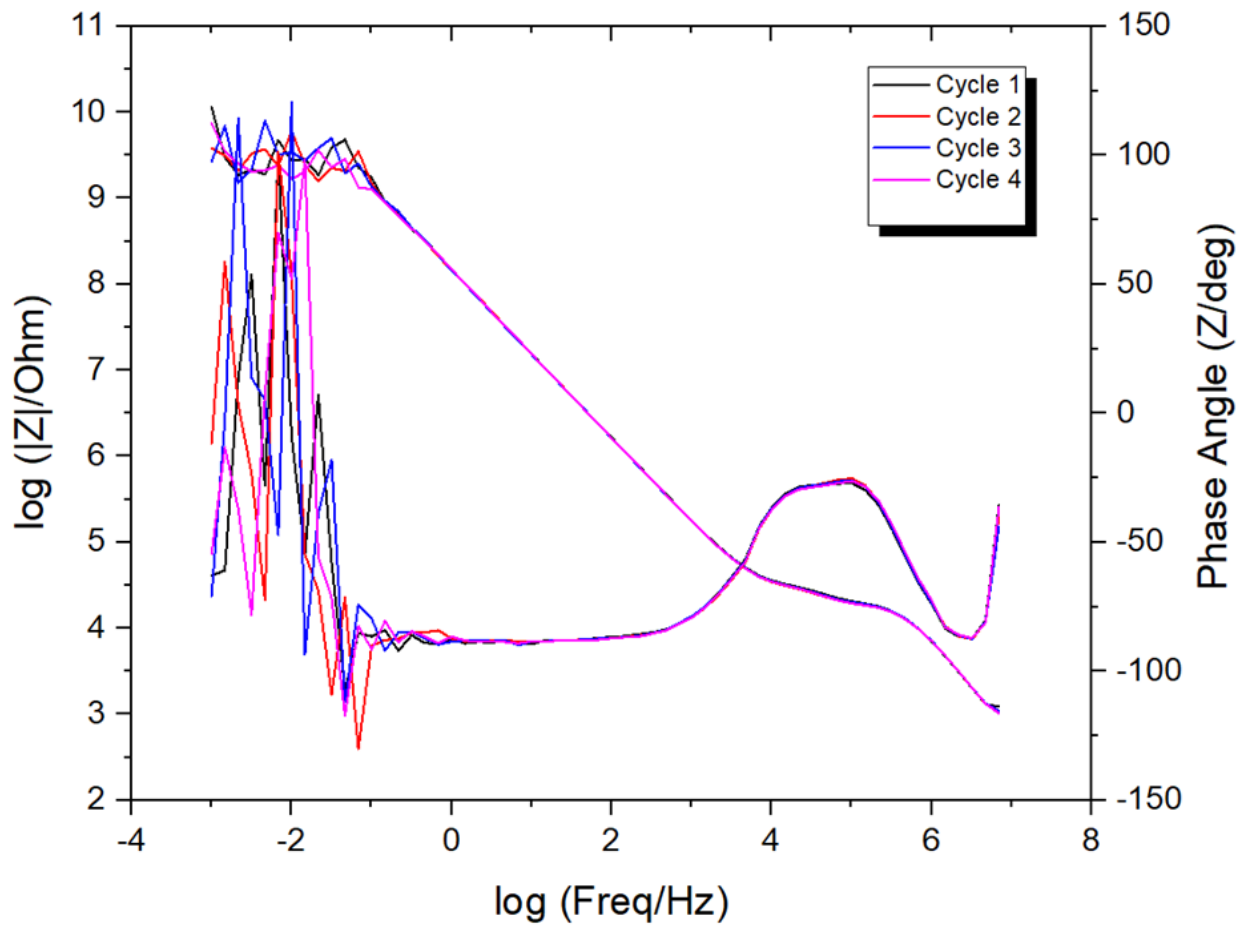
Figure 28   Bode plot for all four cycles of pure zirconium.

4.3.2 Pure Zirconium

For pure zirconium, the produced spectra are almost identical in nature for the first three oxidation states, in both Nyquist and Bode form. This makes sense, as during these oxidation states the oxide is compact and in the pre-breakaway state, and more resistive in nature. Once breakaway is reached, however, at OS4 (oxidized for 113

hours), the resultant impedance experiences a shift in impedance and phase angle.

Referring to the Bode plot in Figure 29, the log impedance experiences a drop of a few

orders of magnitude during the frequency range of 10^{-3} Hz to 10^1 Hz. With increasing

frequency, an overall decrease in impedance is observed, with a defined negative slope

apparent for all four oxidation states during the median frequencies. At the higher

frequency range, around 10^4 Hz, the impedance value for each oxidized sample arrives at

approximately 10^4 Ohms. The phase angle for the pre-breakaway samples remained close

in value with one another, approximately around the -100 Z/deg mark from 10^{-1} to 10^3

Hz. The phase angle "valley" (Or the portion of the phase angle graph that experiences a

local minimum in value), has a large shift for the post-breakaway sample, indicating that

a physical process, or cracking, has occurred in the Zr oxide system. This is

representative, for this scenario, that a breakaway has occurred in the oxide layer.
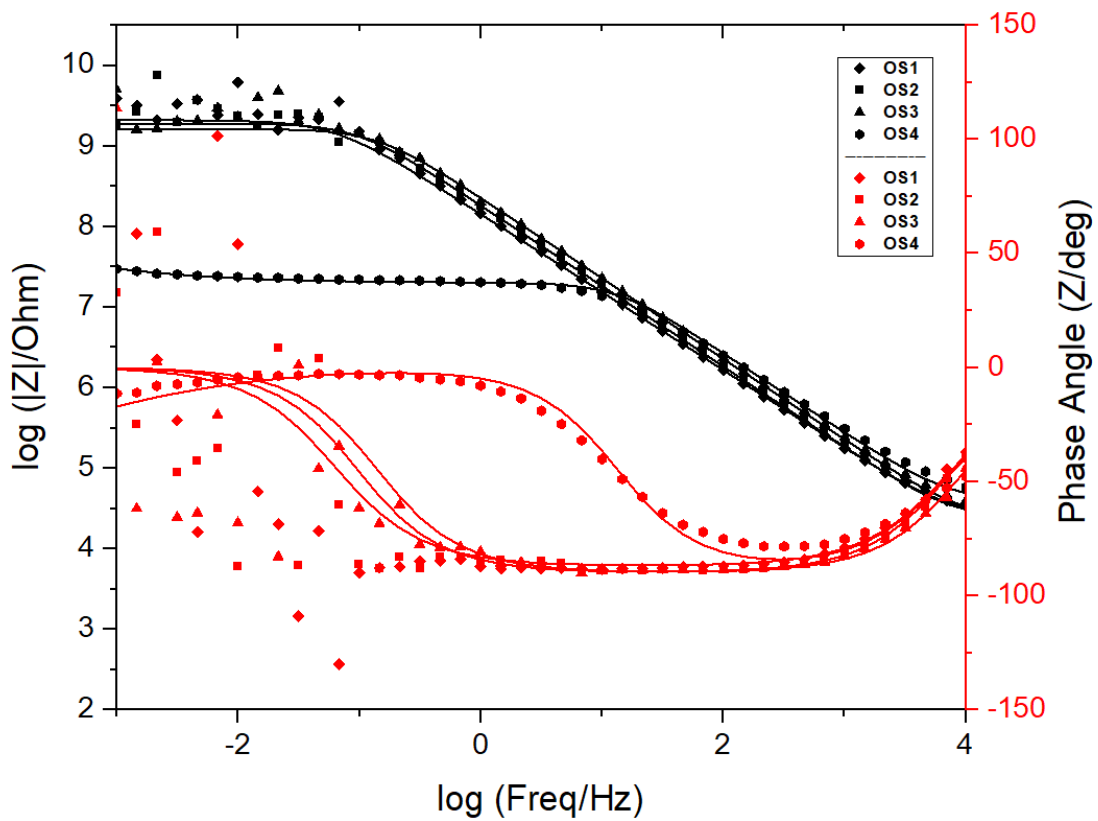
Figure 29 **Bode plot for pure zirconium for oxidation evolution.**

4.3.3 Zry-4

Below in Figure 30, similar plots are presented for the Zry-4 samples. The Bode

plot revealed that as the oxidation state increases, the impedance of the system decreases

when evaluated at lower frequencies. As the extent of oxidation increases, similar trends

and slope changes were seen for each oxidation impedance curve as seen in the pure

zirconium samples. The pre-breakaway sample, at OS1, yielded an impedance of

approximately 10^9 Ohms, with the latter post-breakaway samples reporting at

approximately the 10^7 Ohm mark. The phase angle contained a large amount of variation

for OS1-3 at lower frequencies, but stabilized at the post-breakaway oxide state, towards

10^3- 10^4 Hz. The phase angle valley, however, for each progressing oxidation state shifted right as the oxidation progressed. Impedance data acquired above 10^6 range was not further analyzed since contributions from experimental setup artifacts are difficult to distinguish.
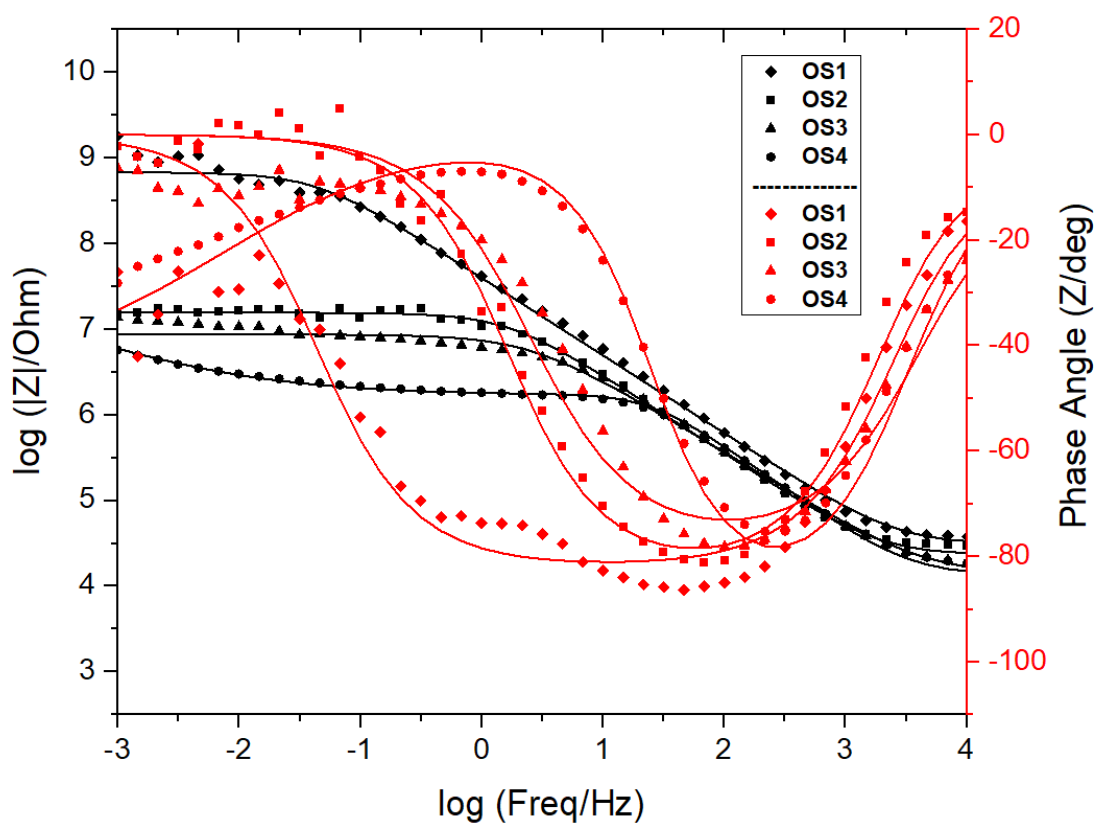
Figure 30   Bode plot for Zry-4 for oxidation evolution.

4.3.4 Zry-2.65Nb

The log impedance on the Bode plot for Zry-2.65Nb samples in Figure 31 decreased as oxidation state progressed, and at the higher frequency range, each oxidation state approached the 10^4 - 10^5 Ohm range. Additionally at this high frequency range, the

impedance curves overlap each other for each oxidation state, and follow a similar decreasing slope in value. For OS1-4, the impedance value decreased from approximately 10^9 - 10^6 Ohms during the lowest frequency range tested, 10^{-3}. This drop in impedance can be attributed to the physical degradation of the oxide, as OS2-4 had experienced severe cracking and warping as they were oxidized.

Observing the trends in the phase angle data, it can be seen that the phase angle increases at lower frequencies as oxidation state progresses. At higher frequencies, the phase angle generally follows a similar trend for each of the oxidation states, yielding similar upward slopes. The relaxation valley for this data set also follows the behavior seen in the Zry-4 and the pure zirconium counterparts, with the local minimum for the valley shifting to the right as OS progresses, and with the slope changes being steeper in their transition.
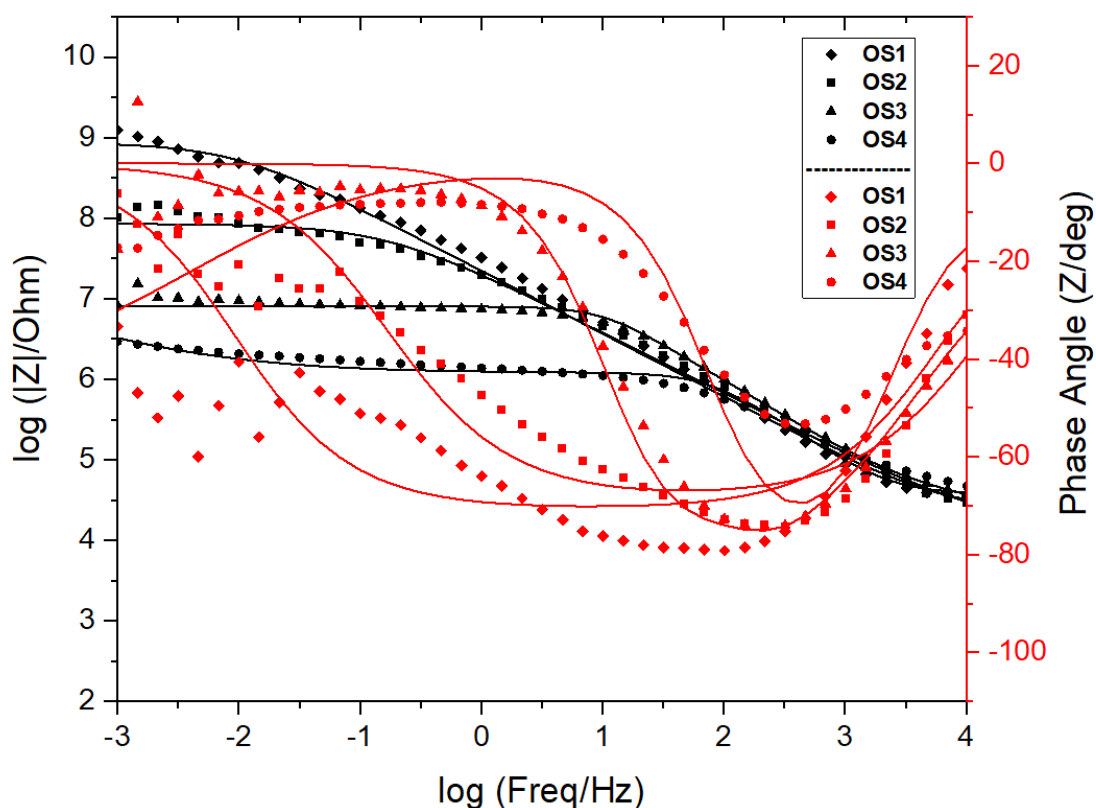
Figure 31   Bode plot for Zry-2.65Nb for oxidation evolution.

4.3.5 Oxide Thickness from Impedance Data

From previous studies, EIS has been utilized as a method to predict the protective

oxide thickness grown on zirconium and zirconium alloys. In order to investigate its

effectiveness for pure zirconium and the alloys investigated in this study, the complex

capacitance and impedance were used to calculate the thickness of the oxidized samples.

The oxide layer can be considered as a pure capacitor at higher frequencies; thus the

impedance was observed at approximately 100 Hz. These thicknesses were then

compared to the thickness values observed from cross sectioned portions of the oxidized

samples in the SEM. Using Equation 7, the complex capacitance was derived from

impedance data and applied to an oxide thickness formula (listed below in Equation 8).

The complex capacitance was calculated using impedance data taken at 101.395 Hz for

the room temperature studies, and 114.232 Hz for the high temperature Zry-4 tests.

$$C(\omega) = \frac{1}{j\omega(Z(\omega) - R_s)}$$

Equation 7: Complex Capacitance at 101.395 Hz [19]

$$d_f = \frac{\varepsilon_0 \varepsilon}{C_f}$$

Equation 8: Oxide Thickness formula [19]

Below in Figure 32, the SEM versus EIS oxide thickness is reported and

compared. For pure zirconium, good agreement was reached for the protective, pre-

breakaway oxidation states (OS1-3), within a few microns of one another. The results for

OS4 for each method, however, had a great disparity present between thicknesses. From

the EIS method, the thickness was estimated to be 29.11 μm, compared to that of the

visual SEM average thickness of 100.67 μm. It is believed this variance could stem from

several different avenues. One similar study [27] reported that EIS oxide thickness

predictions are only valid for zirconium samples still in the pre-breakaway state, and that

once breakaway has occurred, inaccurate thickness measurements are given as a result of

the enhanced kinetics of the system, and the horizontal and vertical cracking present in

the sample. This same study proposes that the oxide value produced at this state is representative of the intact, protective portion of the oxide at the time of measurement, and that once breakaway occurs, the reciprocal capacitance drops to its original value, and disrupts the measurement. Once a protective oxide begins to form again at the oxide/metal interface, the reciprocal capacitance rises again in value, and these values can again be calculated, for the more recently created protective oxide layer.
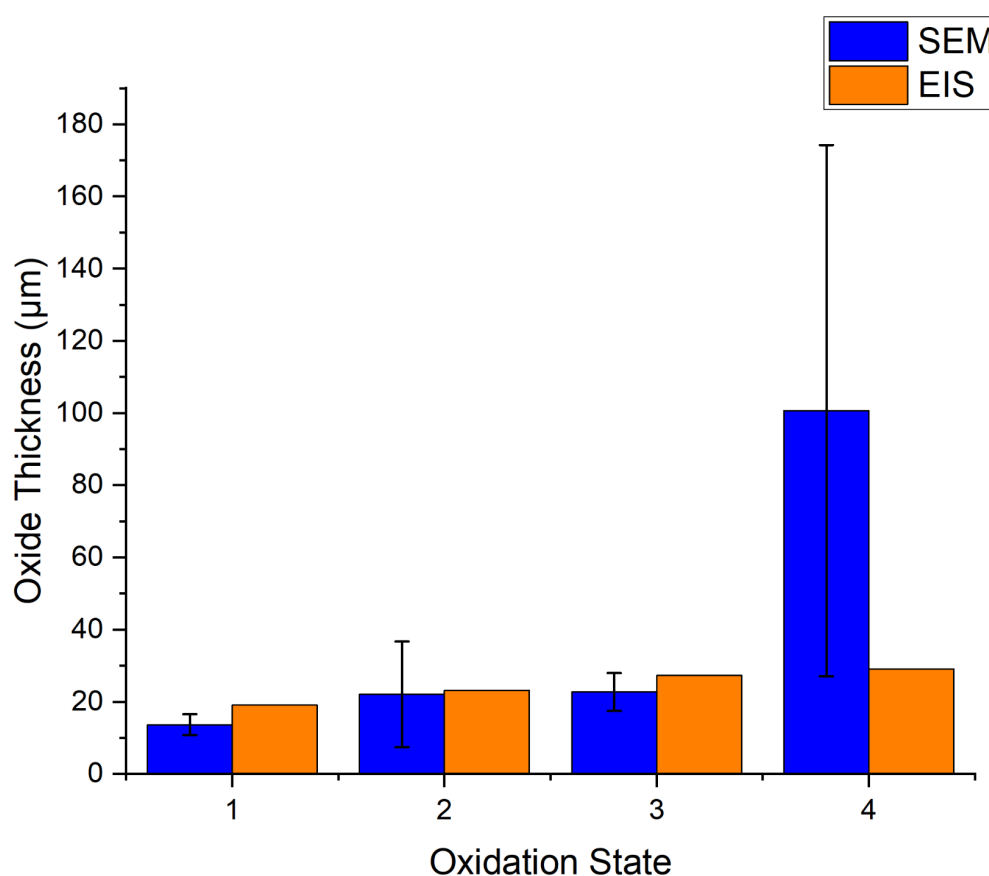
Figure 32   **Oxide thickness for pure zirconium as calculated by SEM and EIS evaluation.**

For the Zry-4 comparisons, agreement was found in that of the pre-breakaway OS1 sample. The estimated value from the SEM analysis vs. the produced EIS value is 6.61 μm and 7.24 μm, respectively A larger variance, however, is recorded in the post-breakaway OS2-4 samples, supporting the trend from the pure zirconium counterparts, and also providing evidence of the oxide transition that has occurred. It is possible that Equations 6-7 do not account for differences in alloying composition, and that different permittivity constants could be contributed from different values.
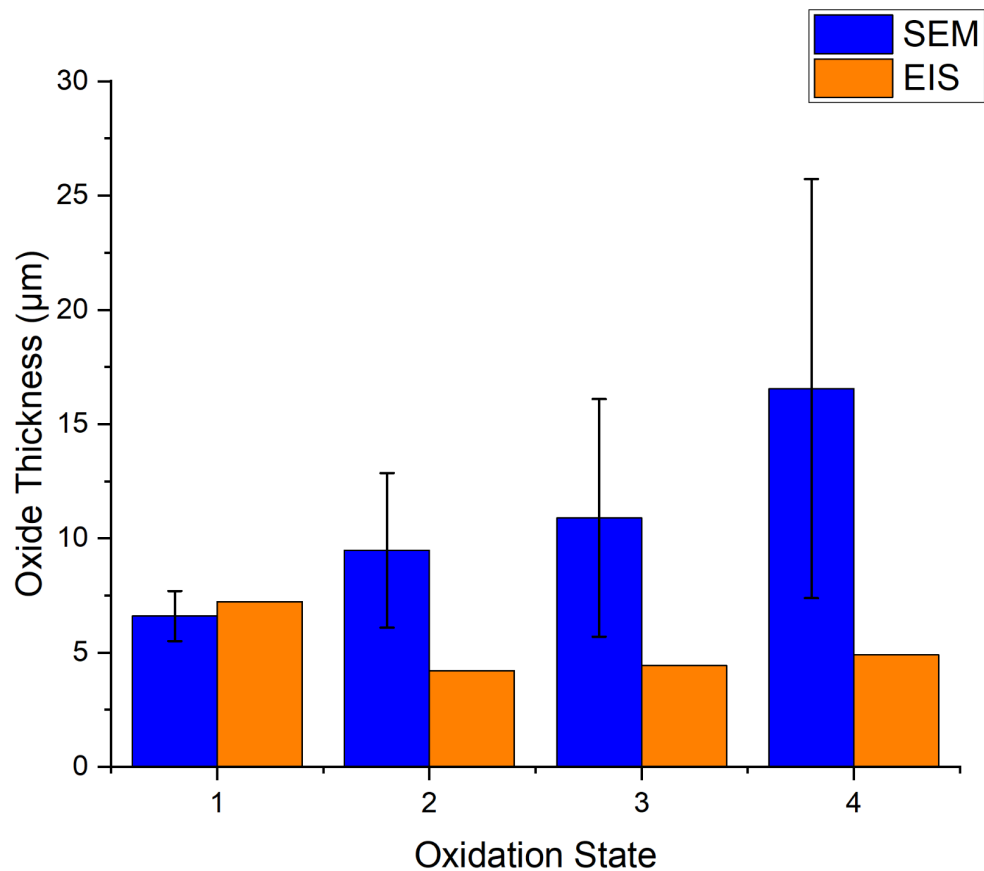
Figure 33 **Oxide thickness for Zry-4 as calculated by SEM and EIS evaluation.**

Below in Figure 34, comparisons for the Zry-2.65Nb samples did not match up as well as the other zirconium alloys. It is expected for OS2-4 to have a large disparity,

since they are quite noticeably in the breakaway state, and experience severe curling

degradation. For OS1, the SEM observed thickness was 21.38 μm, with the EIS

calculated value being only 7.82 μm. This differentiation could be due to inaccurate

assumptions in the used equations surrounding this specific type of zirconium alloy. The

permittivity constant could vary from alloying composition to composition. Additionally,

some slight vertical cracking is observed in the OS1 sample, and it could have already

experienced an oxide transition at this point, altering the capacitance of the oxide and

changing the calculated EIS thickness. It is possible that the OS1 EIS data is reporting the

protective portion of the oxide at this state, and that the cracking distorts the capacitance

value entered into the corresponding equations.

Table 4 below reports on the varying oxide thickness for each alloy, from both the

SEM and EIS perspectives. Zr23 (high temperature Zry-4 sample) also underwent EIS

thickness calculations, and it is included in this table. The generated EIS thickness for

Zr23 was 0.22 μm, compared to the observed thickness of 0.42 μm as seen in the SEM,

with a standard deviation of 0.0516 μm. These results support the argument that these

calculations can be additionally performed at higher operating temperatures and

pressured, with fair accuracy, at 330C and 1875 psi. It is important to note that the oxide

at this point in the experiment was in the pre-breakaway state, also confirming that this

method of oxide thickness prediction serves well for representing a protective oxide
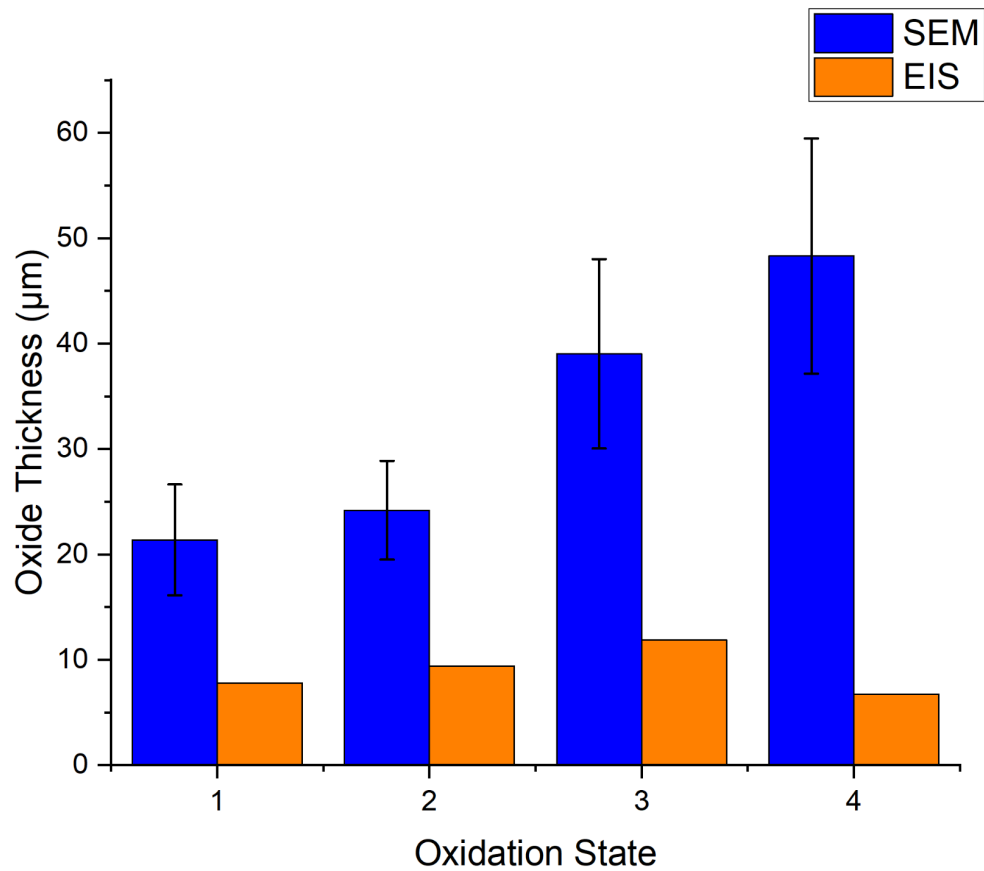
thickness.

Figure 34   **Oxide thickness for Zry-2.65Nb as calculated by SEM and EIS evaluation.**

Table 4   **Average Oxide Thickness Calculated from Impedance Results for Pure Zirconium, Zry-4, Zry-2.65Nb.**

	Pure Zr				Zry-4				Zry-2.65Nb				Zr23
	OS1	OS2	OS3	OS4	OS1	OS2	OS3	OS4	OS1	OS2	OS3	OS4	OS1
EIS average thickness (μm)	19.13	23.22	27.30	29.11	7.24	4.21	4.44	4.90	7.82	9.40	11.87	6.75	0.22
SEM average thickness (μm)	13.66	22.13	22.73	100.67	6.61	9.48	10.90	16.55	21.38	24.20	39.03	48.31	0.42

4.4 Impedance Data for Varying Electrolytes and Alloys

To better understand the effect of electrolyte influence on resultant impedance, several samples of each alloy type were exposed to DI-water, KOH, and LiOH environments during testing. As with the oxidation evaluation, each sample was cycled four times and the second cycle reported in the figures below. The samples used for this portion of the study were all in the un-oxidized state, polished to the 1200 grit polishing step. The Bode representations are recorded below for each electrolyte configuration. The frequency range presented in this section is encompassing the 10^{-3} to 10^4 Hz frequency range.

Overall, the general trends observed over the frequency range tested for the impedance results remain the same for each electrolyte tested. The relaxation valley for the phase angle at lower frequencies for each electrolyte varies, with KOH and LiOH yielding lower values in comparison to the Di-Water test. At 10^{-3} Hz, the impedance experiences a general drop in value going from the LiOH, KOH, and Di-water tests, respectively. Above the 10^4 Hz range, an irregular inflection point is observable for all phase angle and impedance curves, believed to be representative of noise from the testing apparatus. These noticeable disturbances are present for all unfitted Bode plots comparing electrolyte differences.

For Zry-4, similar trends are present over the span of each electrolyte environment tested. A slight drop in impedance is present in high to mid-level frequencies for the KOH test, but lower frequency impedance data are generally similar in value of one another. Additionally, the relaxation valley for the phase angle of the KOH test has a deeper value than that of its other electrolyte counterparts at lower

frequencies. The impedance values at the lowest frequency (10^{-3} Hz) had DI-Water yield the highest impedance value, with KOH and LiOH yielded lower impedances, respectively. For the Nyquist plots in the Appendix section, the impedance values can be seen more clearly over the low and high frequency ranges. Two time constants can be seen at higher frequency ranges, with the KOH test yielded a lower impedance at this range.

The Nyquist plot in the Appendix section at lower frequencies for Zry-2.65Nb yielded almost identical impedance values. At higher frequencies, however, a larger impedance is present for the DI-Water testing conditions. Similarly to that of the pure zirconium testing, two time constants can be observed at higher frequency ranges, and the DI-water experiment yielded the highest of the charge transfer and solution resistances. While the slope changes and inflection points remain the same for each electrolyte, DI-water overall possessed a higher impedance during the test for the majority of the frequency range tested. The final impedance at the 10^{-3} Hz mark, however, yielded almost identical results for each electrolyte tested.

4.4.1 DI-Water

Below, in the following figures, Bode plots are presented to directly compare impedance and phase angle differences between the alloy types. Figure 35 shows the direct comparison for alloys tested in DI-water. The impedance for Zry-4 over the mid frequency range was lower than that of the pure zirconium and Zry-2.65Nb variants, but yielded a higher overall impedance at the 10^{-3} Hz frequency. The phase angle curves each experienced the relaxation valley around the same frequency range (approximately 10^{-2} –

10^{-1} Hz), with the phase angle shift slightly shifted to the right for the pure zirconium sample. For all of the Nyquist plots in the Appendix section, two time constants can be observed at higher frequencies. for each alloy. Specifically, for DI-Water experiments, Zry-4 possessed the lowest value for the charge transfer resistance at higher frequencies, with pure zirconium and Zry-2.65Nb reporting very similar values. Pure zirconium additionally yielded a lower impedance at lower frequency ranges.
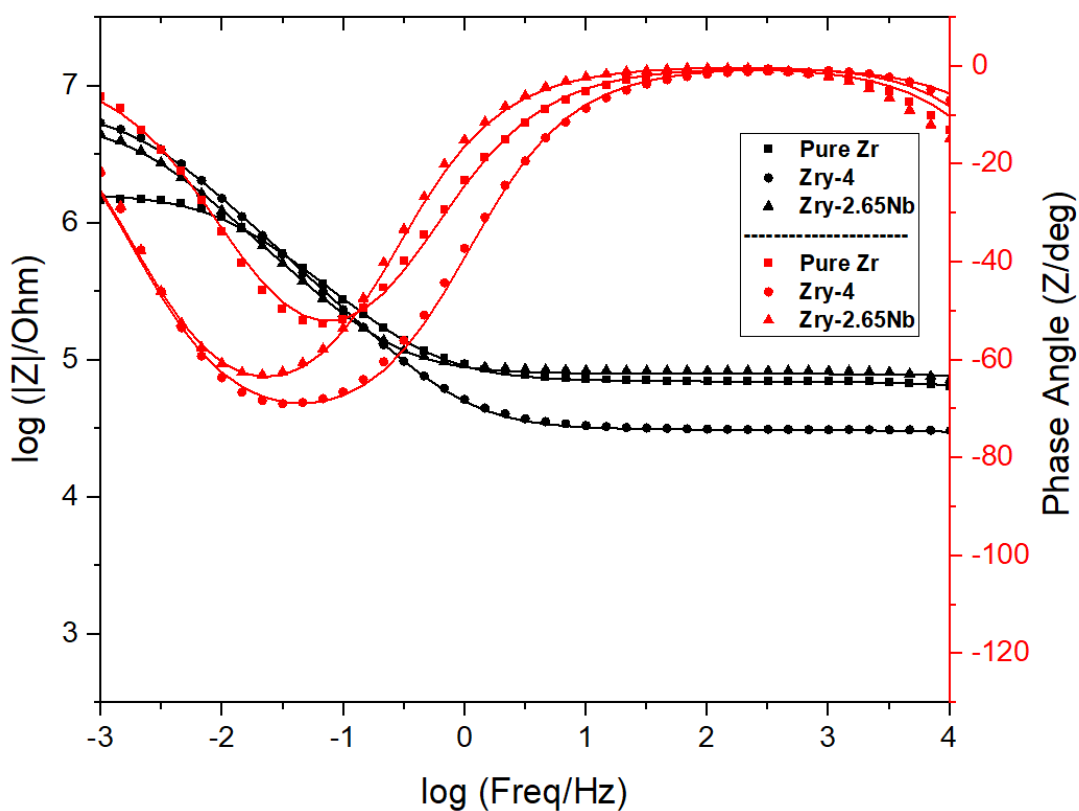
Figure 35   **Bode plot for varying alloys in DI-Water.**

4.4.2 KOH

As seen below in Figure 36, specimens tested in KOH yielded almost identical impedance values at 10^{-3} Hz. At mid-range frequencies, elevated impedance values were observed for pure zirconium, with Zry-4 and Zry-2.65Nb reporting almost identical values. The values for the relaxation valley for Zry-4 and Zry-2.65Nb were very similar with one another, with the pure zirconium sample yielding a slight shift to the left. The Nyquist plots below in the Appendix section report very similar values for the charge transfer resistance of Zry-4 and Zry-2.65Nb at higher frequencies.
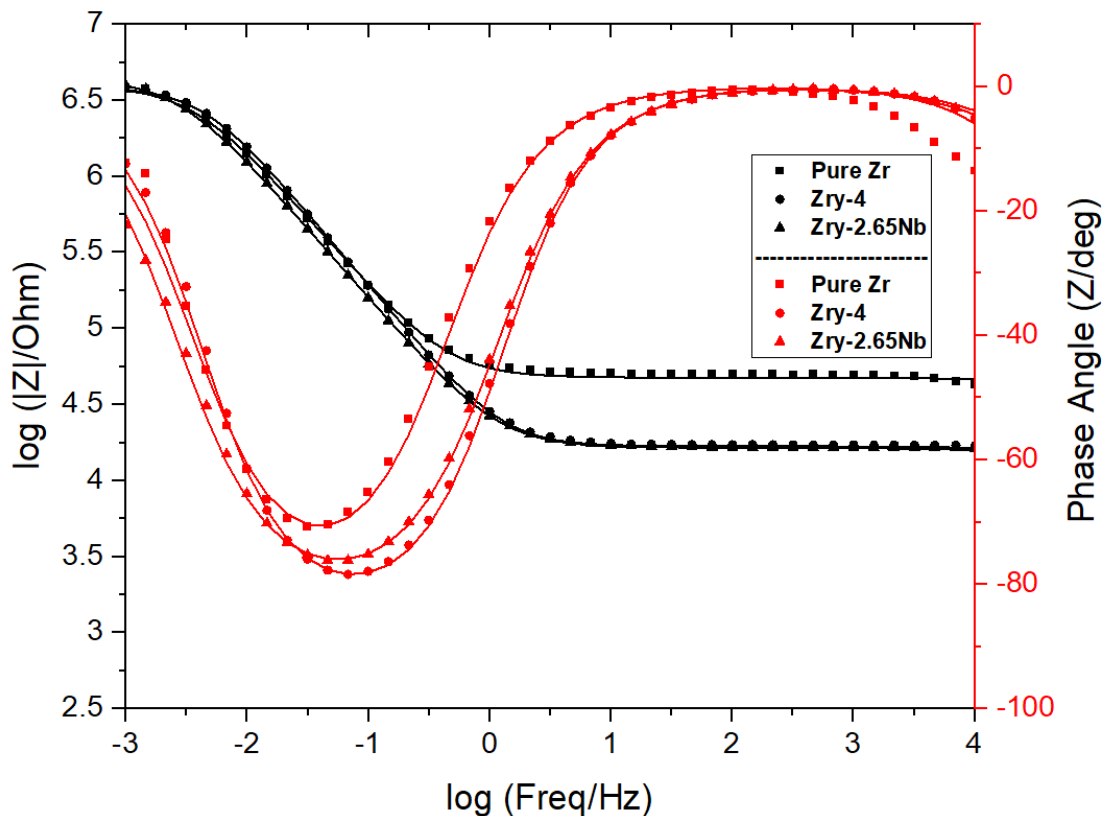
Figure 36   Bode plot for varying alloys in KOH.

4.4.3 LiOH

The impedance values over the mid frequency range for pure zirconium, Zry-4, and Zry-2.65Nb experienced similar trends, but had higher values for that of pure zirconium, then Zry-4 and Zry-2.65Nb, respectively. The phase angle relaxation valley contains a slight shift to the left for pure zirconium, and aligned values for both Zry-4 and Zry-2.65Nb. Charge transfer resistance on the Nyquist plot in the Appendix section decreases from pure zirconium, Zry-4, and Zry-2.65Nb, respectively.
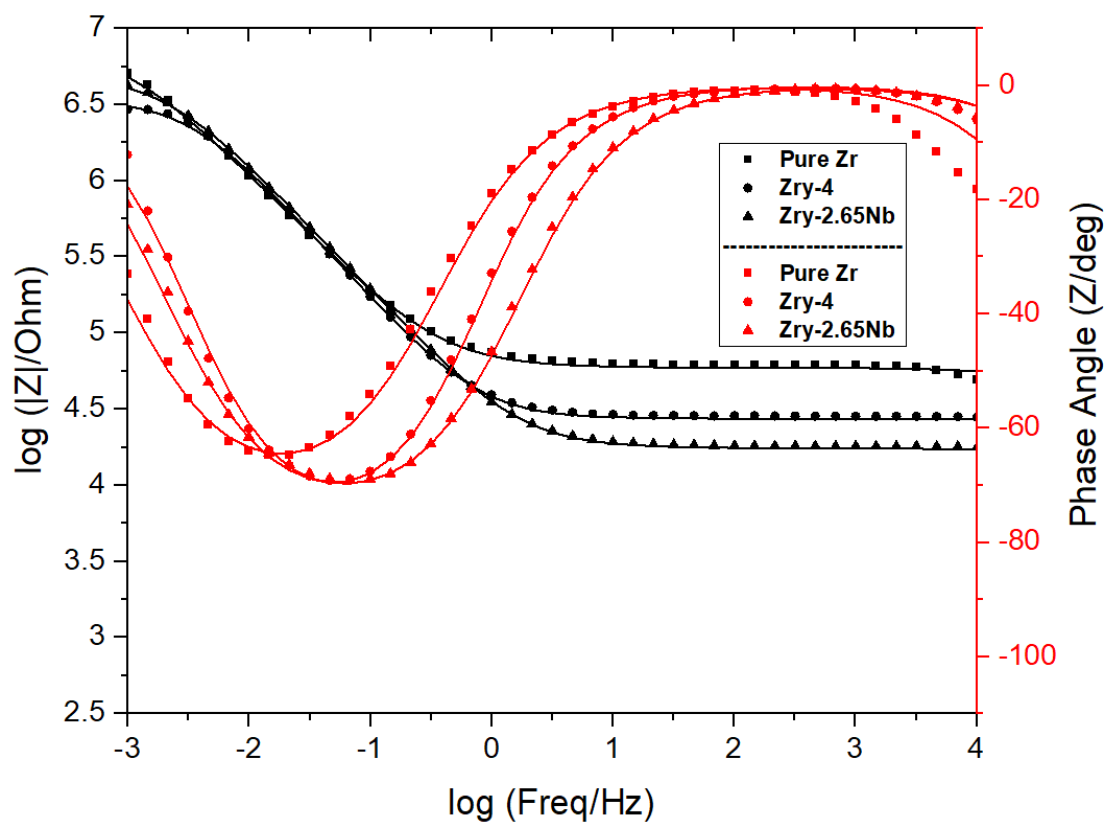
Figure 37   Bode plot for varying alloys in LiOH.

4.5 Impedance Data for Hydrothermal Reactor Specimens

<u>4.5.1 Zry-4 High Temperature, Cycle 31 (Zr22)</u>

Impedance data for the high temperature study is presented below in Figures 38 and 39. Overall, the experimental and fitted data from the equivalent circuit modeling were in good agreement with one another. The Zr22 sample yielded a log |Z| value of around 10^4 Ohm at the lower frequency range, with a lower impedance value of approximately 10^3 Ohm at the higher frequency region. Inside the middle of the frequency range tested ($10^0 – 10^2$ Hz), a gradual drop of impedance can be observed, with a steady negative slope present. The phase angle shift generally remains around the 0-to-20-degree range, with a "relaxation valley" present at approximately 10^1 Hz.
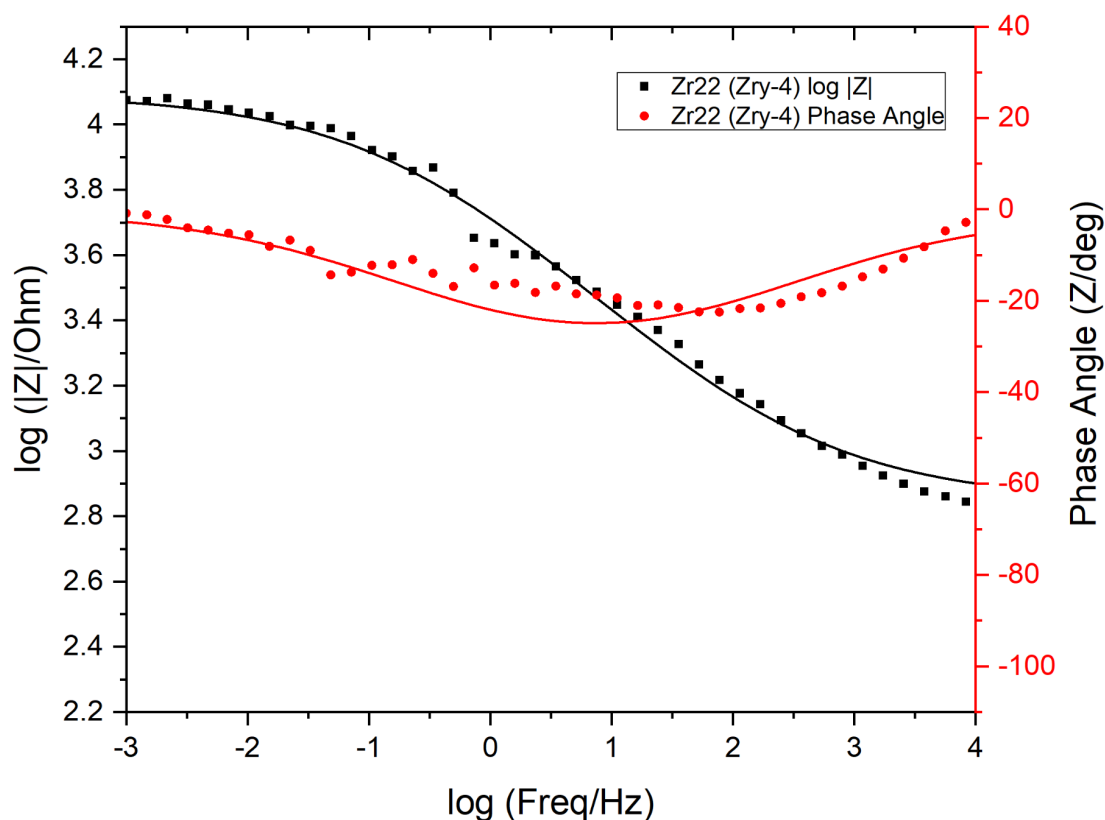
Figure 38   **Bode plot for Zr22 in high temperature environment.**

4.5.2 Zry-4 High Temperature, Cycle 21 (Zr23)

Similar trends that are apparent for sample Zr23 that were present in Zr22. The

log |Z| impedance reaches a value of approximately $10^{3.5}$ Ohms at the high frequency

range, with a drop down to approximately $10^{2.8}$ Ohms at the high frequency region. The

relaxation valley for the phase angle shift is again present at the 10^1 Hz. The lower

modulus of impedance between Zr22 and Zr23 could potentially be attributed to the

slight difference in electrolyte used in the system, with DI-water being utilized instead of

18.2 MΩ millipore water.
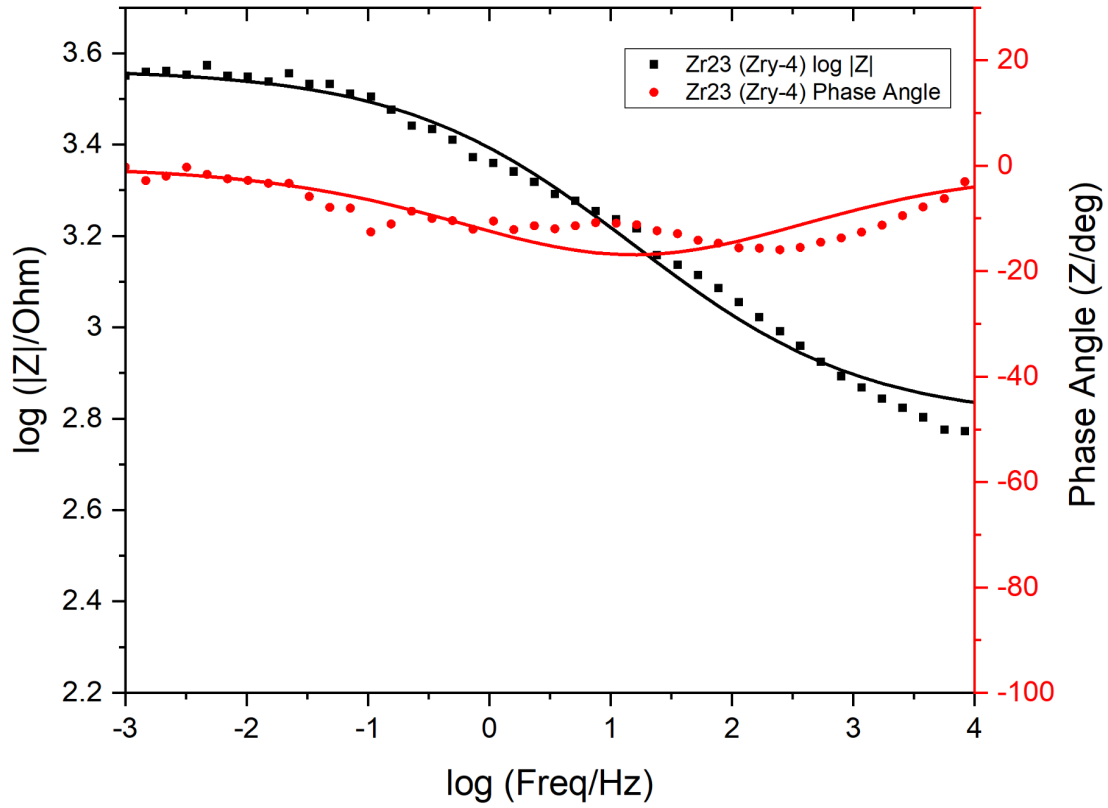
Figure 39   **Bode plot for Zr23 in high temperature environment.**

Renciukova et al. [14] performed a similar EIS study on Zry-4 cladding samples with tubular geometries, and the resultant trends of impedance data and phase angle matched well with the data produced from these two high temperature studies.

CHAPTER 5: CONCLUSIONS

This work utilized Electrochemical Impedance Spectroscopy on both oxidized and unoxidized samples of pure zirconium, Zry-4, and Zry-2.65Nb in varying temperature and environmental states, in an attempt to address four main objectives:

1. Utilize EIS to categorize generated impedance curves based on alloy, electrolyte, oxidation state, and temperature

2. Using this impedance data, compare observed oxide thicknesses via SEM analysis to that of thicknesses calculated from EIS calculations

3. Provide groundwork and proof of concept results to support the development of potential in-situ EIS sensing system

4. Relate resultant impedance data to physical processes occurring within the zirconium oxide system, to form a better understand the corrosion and degradation of the zirconium cladding material system.

For the oxidized samples, zirconium alloys were placed in dry air (N_2 + 20% O_2) at 700°C at varying times to generate different stages of oxidation, some being in the pre-transition regime, and others in the post-transition regime. These samples were EIS tested, and resultant curves reported. In general, impedance drops orders of magnitude as oxidation state progresses, regardless of alloying type. This is an indication, too, of the physical state of the oxide, as capacitance drops once breakaway has been reached. The

phase angle shift reported in the Bode plots for these samples also shifts in accordance with oxide growth. As oxidation state progresses, and grows thicker, the resultant phase angle "valley" will increase accordingly, and shift more toward lower frequencies, indicating that the state of the oxide is evolving within the material system. Direct comparisons between pure zirconium and its alloyed counterparts show that during the pre-transition state, an initial impedance of approximately 10^9 Ohms is present, then decreases to approximately 10^7 Ohms for samples in the post-breakaway state, for each alloying type.

Thickness data calculated from EIS analysis were in good agreement for samples in the pre-transition oxidation regime. Additional correlations were made in comparison with SEM analysis for pre-breakaway zirconium, with larger disparities between calculated and observed thickness present in the post-breakaway samples. Evolution in oxide thickness is attributed to the physical degradation of the oxide, and large drop in oxide resistivity. As reported in previous works, it is suggested that this oxide thickness measurement technique is best used to report on the intact, protective oxide rather than the porous, post-breakaway state. Thickness measurements on the high temperature tested Zry-4 were also close in agreement, revealing that higher temperature testing is also viable for in-situ sensing applications.

Differences in electrolyte contributions for non-oxidized samples were also investigated in this work, by dissecting produced Bode plots. Di-Water, LiOH, and KOH water chemistries were evaluated due to their prominence in LWR reactor environments. For DI-Water, at the lower 10^{-3} Hz frequency, EIS spectra yielded very similar impedances for Zry-4 and Zry-2.65Nb samples (at approximately 10^7 Ohms), with a

lower impedance for pure zirconium (approximately 10^6 Ohms). At the mid to higher frequency ranges, the impedance plateaus out for each sample, with Zry-4 yielded a lower overall impedance than its other counterparts. The phase angle valley for each sample lie in close proximity of each other in between the $10^{-2} – 10^{-1}$ Hz frequency range, with the phase angle well having a higher value for that of pure zirconium. For KOH tests, at low frequencies all samples yielded almost identical impedances, with pure zirconium yielding a higher impedance at mid to higher frequencies. The phase angle valley for samples tested in KOH were lower in value than that of the DI-Water tests but experienced the phase angle well at a similar frequency range. For the LiOH tests, again, similar impedance values are reported for each alloy at the low 10^{-3} Hz range, with impedances of approximately $10^{6.5}$ Ohms present. Pure zirconium again yields a higher impedance than that of the other alloys at the mid to higher frequency range. Deeper wells in the phase angle plots can be seen for the LiOH and KOH runs, but no other significant differences can truly be discerned from the electrolyte testing, indicating that higher concentrations of electrolyte may be studied in the future to help better categorize generated EIS curves, and to assist in revealing any other produced trends due to electrolyte interactions with the material system.

CHAPTER 6. FUTURE WORK

The general purpose of this work, not including the contribution to the understanding of zirconium oxide structure and impedance properties, is to support the design of an in-situ EIS based sensor to be used as an active fuel cladding monitoring system. By observing generated curves while in-pile, operators can identify when a LWR may need to be pulled offline for maintenance and repair. This sensing system could potentially save the nuclear energy industry in start-up / shutdown costs, which can take considerable amounts of time and effort in performing. Below in Figure 40 is a preliminary Solidworks 3D model with associated dimensions of an in-core sensor prototype. This design calls for several alumina tubes to serve as a housing for the wiring to the electrodes. A network array of EIS sensors placed evenly around the fuel bundles could provide a comprehensive, real-time status of the components throughout the core. Innovation time for nuclear hardware is a difficult issue to tackle, however, due to the amount of time it takes to get a new piece of equipment inside of a test reactor. Longer duration tests are needed to ensure the integrity of the new technology being proposed, and perhaps testing these zirconium alloy systems for extended periods of times could lead to more accurate evidence of cladding health in generated impedance curves. Further, introducing a recirculating loop system into the hydrothermal reactor that provides continually circulating primary water into the vessel might be needed for extended duration testing, rather than the static environment used in this work.
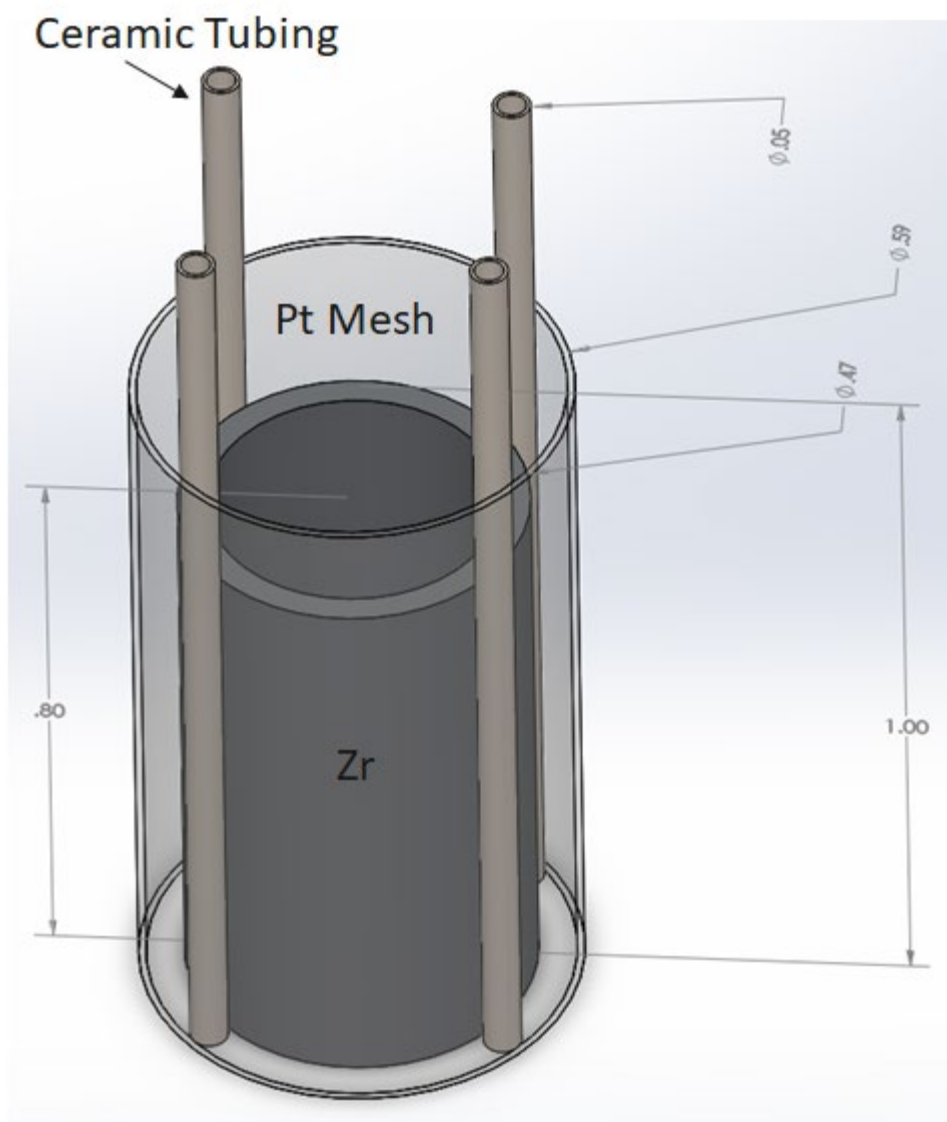
Figure 40   Solidworks projection for a potential in-situ EIS configuration, with dimensions in inches.

Further testing at elevated temperatures, with more controlled pressure levels, could prove to be beneficial in adding to the literature of in-situ EIS data. In this work, only LiOH was used for the hydrothermal reactor runs, so other LWR water chemistries, potentially with varying concentrations, could be tested and the resultant impedance curves could be categorized for analysis. Additionally, the co-axially aligned

experimental setup used in the hydrothermal evaluations could also be used in the room temperature testing. This way, more accurate comparisons might be able to be made between the two, removing the variability of cell geometry.

Testing samples that have been exposed to radiation would be another further step to take, and some work has been done that evaluates Zry-4 and the M5 zirconium variant [44]. It is hard to predict how this type of environment would disturb live impedance data, but perhaps irradiated samples could be analyzed first, with a fixture being placed in a test reactor to evaluate said conditions. Despite these future scientific challenges, EIS has been proven in literature and from this work as a viable method for monitoring fuel cladding functionality and provided new insight to support progression in nuclear sensing technology.

REFERENCES

[1]   Motta, Arthur T., et al. "Corrosion of Zirconium Alloys Used for Nuclear Fuel Cladding." *Annual Review of Materials Research*, vol. 45, no. 1, 2015, pp. 311–343., https://doi.org/10.1146/annurev-matsci-070214-020951.

[2]   Lustman B. 1979. Zirconium technology—twenty years of evolution. In 4th International Symposium on Zirconium in the Nuclear Industry, ASTM STP 681, pp. 5–18. West Conshohocken, PA: ASTM Int.

[3]   Rickover HG, Geiger LD, Lustman B. 1975. History of the development of zirconium alloys for use in nuclear reactors. Rep., Energy Res. Dev. Admin./Div. Naval React., Washington, DC

[4]   Steuwer, A., Santisteban, J.R., Preuss, M., Peel, M.J., Buslaps, T., Harada, M. "Evidence of Stress-Induced Hydrogen Ordering in Zirconium Hydrides." *Acta Materialia*, vol. 57, no. 1, 2009, pp. 145–152., https://doi.org/10.1016/j.actamat.2008.08.061.

[5]   Oskarsson, M., et al. "Oxidation of Zircaloy-2 and Zircaloy-4 in Water and Lithiated Water at 360°C." *Journal of Nuclear Materials*, vol. 295, no. 1, 2001, pp. 97–108., https://doi.org/10.1016/s0022-3115(01)00480-9.

[6]   Chu, H.c., et al. "Effect of Radial Hydrides on the Axial and Hoop Mechanical Properties of Zircaloy-4 Cladding." *Journal of Nuclear Materials*, vol. 362, no. 1, 2007, pp. 93–103., https://doi.org/10.1016/j.jnucmat.2006.11.008.

[7]   Vermoyal, J.j., et al. "AC Impedance Study of Corrosion Films Formed on Zirconium Based Alloys." *Electrochimica Acta*, vol. 45, no. 7, 1999, pp. 1039–1048., https://doi.org/10.1016/s0013-4686(99)00307-2.

[8]   Vermoyal, J.j., et al. "In Situ Characterization of Zircaloy-4 Oxidation at 500 °C in Dry Air." *Journal of Nuclear Materials*, vol. 298, no. 3, 2001, pp. 297–308., https://doi.org/10.1016/s0022-3115(01)00648-1.

[9]   Vermoyal, J.j, et al. "Electrical Characterization of Waterside Corrosion Films Formed on ZrNb(1%)O(0.13%)." *Electrochimica Acta*, vol. 47, no. 17, 2002, pp. 2679–2695., https://doi.org/10.1016/s0013-4686(02)00133-0.

[10]   Vermoyal, J.j, et al. "Contribution to the Understanding of the ZrNb(l%)O(0.13%) Oxidation Mechanism at 500 °C in Dry Air." *Journal of Nuclear Materials*, vol. 328, no. 1, 2004, pp. 31–45., https://doi.org/10.1016/j.jnucmat.2004.02.013.

[11]   Nagy, Gabor, et al. "In Situ Electrochemical Impedance Spectroscopy of Zr–1%Nb under VVER Primary Circuit Conditions." *Journal of Nuclear Materials*, vol. 300, no. 2-3, 2002, pp. 230–236., https://doi.org/10.1016/s0022-3115(01)00735-8.

[12]   Schiller, Robert, et al. "Continuous-Time Random-Walk Theory of Interfering Diffusion and Chemical Reaction with an Application to Electrochemical Impedance Spectra of Oxidized Zr–1%Nb." *The Journal of Chemical Physics*, vol. 123, no. 9, 2005, p. 094704., https://doi.org/10.1063/1.1949165.

[13]   Macák, Jan, et al. "Electrochemical Study of Pre - and Post-Transition Corrosion of Zr Alloys in PWR Coolant." *15th International Conference on Environmental Degradation of Materials in Nuclear Power Systems-Water Reactors*, 2012, pp. 655–663., https://doi.org/10.1002/9781118456835.ch68.

[14]   Renčiuková, Veronika, et al. "Corrosion of Zirconium Alloys Demonstrated by Using Impedance Spectroscopy." *Journal of Nuclear Materials*, vol. 510, 2018, pp. 312–321., https://doi.org/10.1016/j.jnucmat.2018.08.005.

[15]   Krausová, Aneta, et al. "In-Situ Electrochemical Study of Zr1nb Alloy Corrosion in High Temperature Li Containing Water." *Journal of Nuclear Materials*, vol. 467, 2015, pp. 302–310., https://doi.org/10.1016/j.jnucmat.2015.10.005.

[16]   Bojinov, Martin, et al. "Influence of Water Chemistry on the Corrosion Mechanism of a Zirconium–Niobium Alloy in Simulated Light Water Reactor Coolant Conditions." *Corrosion Science*, vol. 52, no. 1, 2010, pp. 54–67., https://doi.org/10.1016/j.corsci.2009.08.045.

[17]   Bojinov, Martin, et al. "In-Situ Studies of the Oxide Film Properties on BWR Fuel Cladding Materials." *Zirconium in the Nuclear Industry: Fourteenth International Symposium*, https://doi.org/10.1520/stp37516s.

[18]   Bojinov, Martin, et al. "Kinetic Parameters of the Oxidation of Zirconium Alloys in Simulated WWER Water – Effect of KOH Content." *Journal of Nuclear Materials*, vol. 378, no. 1, 2008, pp. 45–54., https://doi.org/10.1016/j.jnucmat.2008.04.014.

[19]   Benoit, Marie, et al. "Comparison of Different Methods for Measuring the Passive Film Thickness on Metals." *Electrochimica Acta*, vol. 201, 2016, pp. 340–347., https://doi.org/10.1016/j.electacta.2015.12.173.

[20]   Bataillon, C., and S. Brunet. "Electrochemical Impedance Spectroscopy on Oxide Films Formed on Zircaloy 4 in High Temperature Water." *Electrochimica Acta*, vol. 39, no. 3, 1994, pp. 455–465., https://doi.org/10.1016/0013-4686(94)80086-3.

[21]   Durand-Keklikian, L., et al. "Ex Situ A.C. Impedance Studies of Oxide Film Growth on Zircaloys in High Temperature/High Pressure Steam." *Corrosion Science*, vol. 32, no. 3, 1991, pp. 347–359., https://doi.org/10.1016/0010-938x(91)90079-5.

[22]   Durand-Keklikian, L., et al. "In Situ A.C. Impedance Studies of Oxide Film Growth on Zircaloy-4 in High Temperature/High Pressure Steam." *Corrosion Science*, vol. 32, no. 3, 1991, pp. 361–365., https://doi.org/10.1016/0010-938x(91)90080-9.

[23]   Barberis, P., and A. Frichet. "Characterization of Zircaloy-4 Oxide Layers by Impedance Spectroscopy." *Journal of Nuclear Materials*, vol. 273, no. 2, 1999, pp. 182–191., https://doi.org/10.1016/s0022-3115(99)00025-2.

[24] Forsberg, S., et al. "Studies of Corrosion of Cladding Materials in Simulated BWR Environment Using Impedance Measurements." *Journal of ASTM International*, vol. 4, no. 9, 2007, p. 101123., https://doi.org/10.1520/jai101123.

[25] Schefold, J., et al. "The Cyclic Nature of Corrosion of Zr and Zr-Sn in High-Temperature Water (633 K)." *Journal of The Electrochemical Society*, vol. 150, no. 10, 2003, https://doi.org/10.1149/1.1602079.

[26] Ai, Jiahe, et al. "Electrochemical Impedance Spectroscopic Study of Passive Zirconium." *Journal of The Electrochemical Society*, vol. 154, no. 1, 2007, https://doi.org/10.1149/1.2374946.

[27] Couet, Adrien, et al. "In-Situ Electrochemical Impedance Spectroscopy Measurements of Zirconium Alloy Oxide Conductivity: Relationship to Hydrogen Pickup." *Corrosion Science*, vol. 119, 2017, pp. 1–13., https://doi.org/10.1016/j.corsci.2016.12.008.

[28] Ni, N., et al. "How the Crystallography and Nanoscale Chemistry of the Metal/Oxide Interface Develops during the Aqueous Oxidation of Zirconium Cladding Alloys." *Acta Materialia*, vol. 60, no. 20, 2012, pp. 7132–7149., https://doi.org/10.1016/j.actamat.2012.09.021.

[29] Cox, B. "Environmentally-Induced Cracking of Zirconium Alloys — A Review." *Journal of Nuclear Materials*, vol. 170, no. 1, 1990, pp. 1–23., https://doi.org/10.1016/0022-3115(90)90321-d.

[30] Kofstad, Per, and C. A. Steidel. "High Temperature Oxidation of Metals." *Journal of The Electrochemical Society*, vol. 114, no. 7, 1967, https://doi.org/10.1149/1.2426698.

[31] Wikmark, G, et al. "The Importance of Oxide Morphology for the Oxidation Rate of Zirconium Alloys." *Zirconium in the Nuclear Industry: Eleventh International Symposium*, https://doi.org/10.1520/stp16167s.

[32]   Zhang, H.x., et al. "Crystal Structure, Corrosion Kinetics of New Zirconium Alloys and Residual Stress Analysis of Oxide Films." *Journal of Nuclear Materials*, vol. 396, no. 1, 2010, pp. 65–70., https://doi.org/10.1016/j.jnucmat.2009.10.055.

[33]   Liu, Wenqing, et al. "Detrimental Role of LiOH on the Oxide Film Formed on Zircaloy-4." *Corrosion Science*, vol. 47, no. 7, 2005, pp. 1855–1860., https://doi.org/10.1016/j.corsci.2004.08.003.

[34]   Polatidis, E., et al. "Residual Stresses and Tetragonal Phase Fraction Characterisation of Corrosion Tested Zircaloy-4 Using Energy Dispersive Synchrotron X-Ray Diffraction." *Journal of Nuclear Materials*, vol. 432, no. 1-3, 2013, pp. 102–112., https://doi.org/10.1016/j.jnucmat.2012.07.025.

[35]   Yilmazbayhan, Aylin, et al. "Structure of Zirconium Alloy Oxides Formed in Pure Water Studied with Synchrotron Radiation and Optical Microscopy: Relation to Corrosion Rate." *Journal of Nuclear Materials*, vol. 324, no. 1, 2004, pp. 6–22., https://doi.org/10.1016/j.jnucmat.2003.08.038.

[36]   Wadman, B, et al. "Microstructure of Oxide Layers Formed During Autoclave Testing of Zirconium Alloys." *Zirconium in the Nuclear Industry: Tenth International Symposium*, https://doi.org/10.1520/stp15210s.

[37]   Abolhassani, S., et al. "Examination of the Chemical Composition of Irradiated Zirconium Based Fuel Claddings at the Metal/Oxide Interface by TEM." *Journal of Nuclear Materials*, vol. 399, no. 1, 2010, pp. 1–12., https://doi.org/10.1016/j.jnucmat.2009.10.060.

[38]   Bossis, P, et al. "Multi-Scale Characterization of the Metal-Oxide Interface of Zirconium Alloys." *Zirconium in the Nuclear Industry: Twelfth International Symposium*, https://doi.org/10.1520/stp14334s.

[39]   Gou, Shaoqiu, et al. "Investigation of Oxide Layers Formed on Zircaloy-4 Coarse-Grained Specimens Corroded at 360°C in Lithiated Aqueous Solution." *Corrosion Science*, vol. 92, 2015, pp. 237–244., https://doi.org/10.1016/j.corsci.2014.12.012.

[40]   Efaw, Corey M., et al. "Characterization of Zirconium Oxides Part I: Raman Mapping and Spectral Feature Analysis." *Nuclear Materials and Energy*, vol. 21, 2019, p. 100707., https://doi.org/10.1016/j.nme.2019.100707.

[41]   Efaw, Corey M., et al. "Characterization of Zirconium Oxides Part II: New Insights on the Growth of Zirconia Revealed through Complementary High-Resolution Mapping Techniques." *Corrosion Science*, vol. 167, 2020, p. 108491., https://doi.org/10.1016/j.corsci.2020.108491.

[42]   Garner, A., et al. "The Microstructure and Microtexture of Zirconium Oxide Films Studied by Transmission Electron Backscatter Diffraction and Automated Crystal Orientation Mapping with Transmission Electron Microscopy." *Acta Materialia*, vol. 80, 2014, pp. 159–171., https://doi.org/10.1016/j.actamat.2014.07.062

[43]   Vandegrift, Jordan L., et al. "Oxidation Behavior of Zirconium, Zircaloy-3, Zircaloy-4, Zr-1Nb, and Zr-2.5Nb in Air and Oxygen." *Nuclear Materials and Energy*, vol. 20, 2019, p. 100692., https://doi.org/10.1016/j.nme.2019.100692

[44]   Tupin, M., Verlet, R., Wolski, K., Miro, S., Baldacchino, G., Jublot, M., Colas, K., Bossis, P., Ambard, A., Kaczorowski, D., Blat-Yrieix, M., & Idarraga, I. (2018). Understanding of corrosion mechanisms after irradiation: Effect of ion irradiation of the oxide layers on the corrosion rate of M5. *Zirconium in the Nuclear Industry: 18th International Symposium*, 415–447. https://doi.org/10.1520/stp159720160081

APPENDIX

In this section, additional results and supporting analysis obtained from this work are presented. Below in Figure A.1, the four impedance curves for each of the four oxidation states are presented. Here, the initial impedance curve contains an overall higher impedance, as well as an increased charge transfer resistance, as observed from its Nyquist curve hump. The next three curves settle out with similar values of impedance, indicating that the system has stabilized out and reached a steady state.

For Figures A.2 through A.4, Nyquist plots are presented for the oxidation progression of each alloy. Figures A.5 through A.7 report Nyquist plots for each alloy versus varying electrolytes. Figures A.8 through A.10 show the unfitted Nyquist plots for varying alloys in DI-Water, KOH, and LiOH, respectively. Figures A.11 through A.13 report the fitted versions of the Nyquist plots for varying alloys in each respective electrolyte. Figure A.14 reports the unfitted Nyquist curve for the final cycle of sample Zr22, with the fitted Bode plots for each alloy in each electrolyte reported in Figures A.15-A.17.

Figure A.   Nyquist Plots for all four cycles of pure zirconium.

Figure A.2   Nyquist Plots for oxidation progression of pure zirconium.
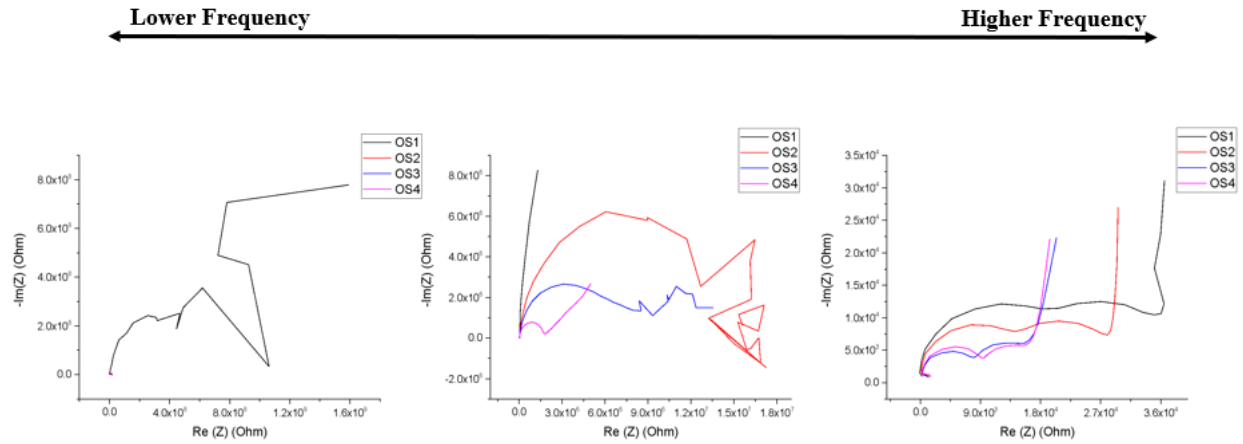
Figure A.3   Nyquist Plots for oxidation progression of Zry-4.
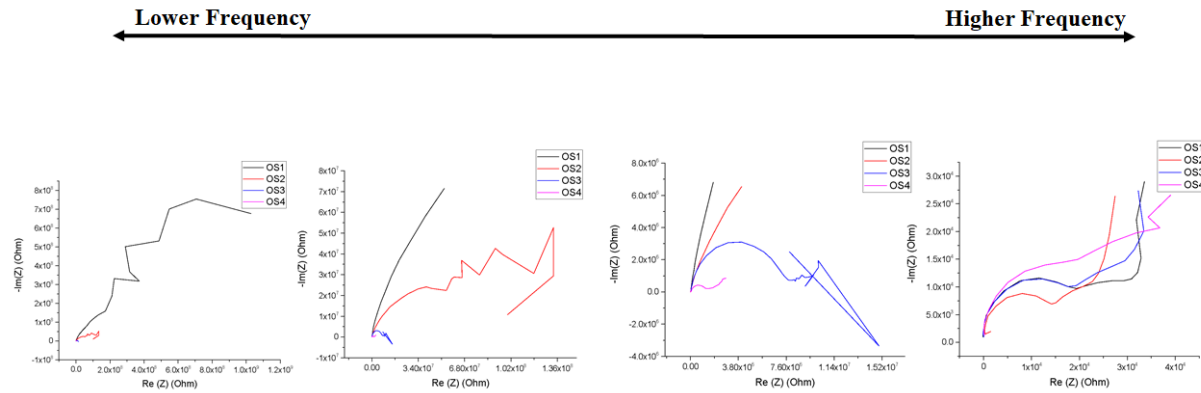
Figure A.4   Nyquist Plots for oxidation progression of Zry-2.65Nb.
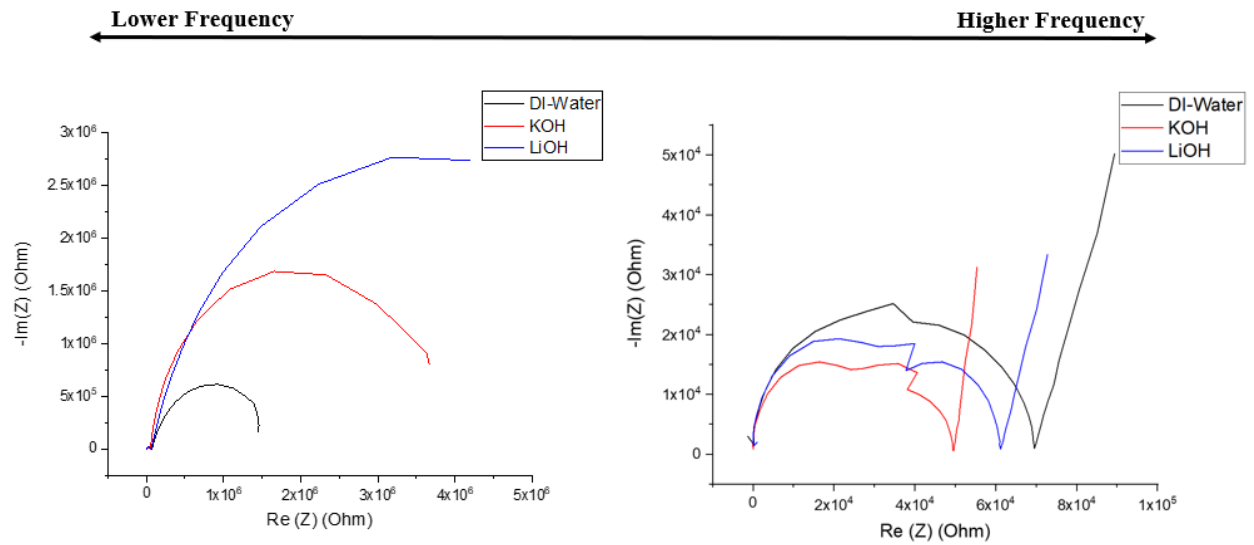
Figure A.5   Nyquist plots for Pure Zirconium in varying electrolytes.

Figure A.6   Nyquist plots for Zry-4 in varying electrolytes.

Figure A.7   Nyquist plots for Zry-2.65Nb in varying electrolytes.
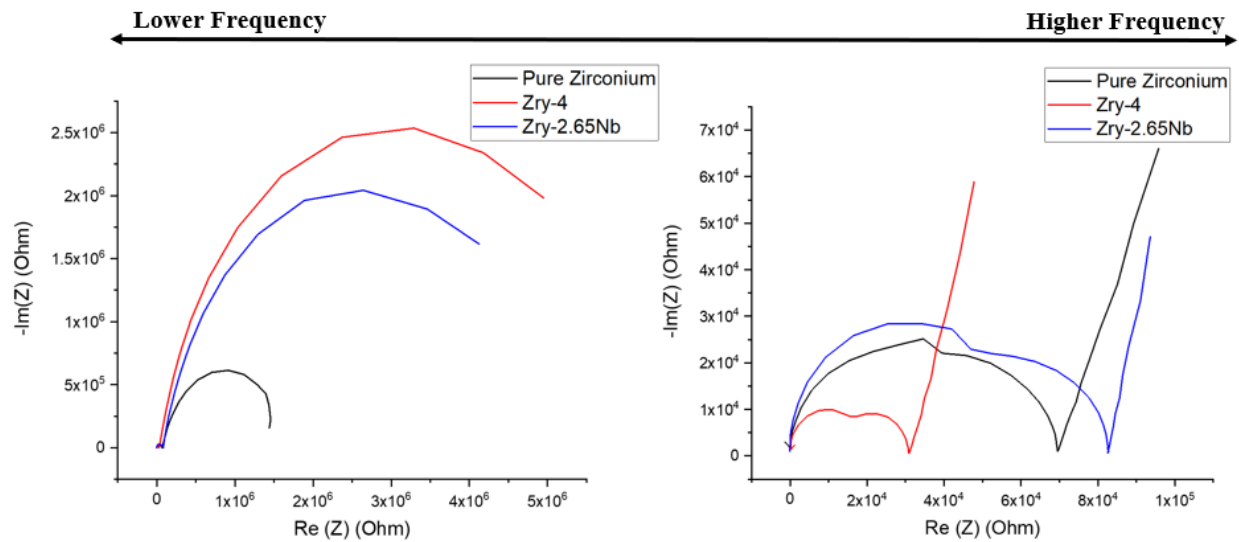
Figure A.8   Unfitted Nyquist plots for varying alloys in DI-Water.
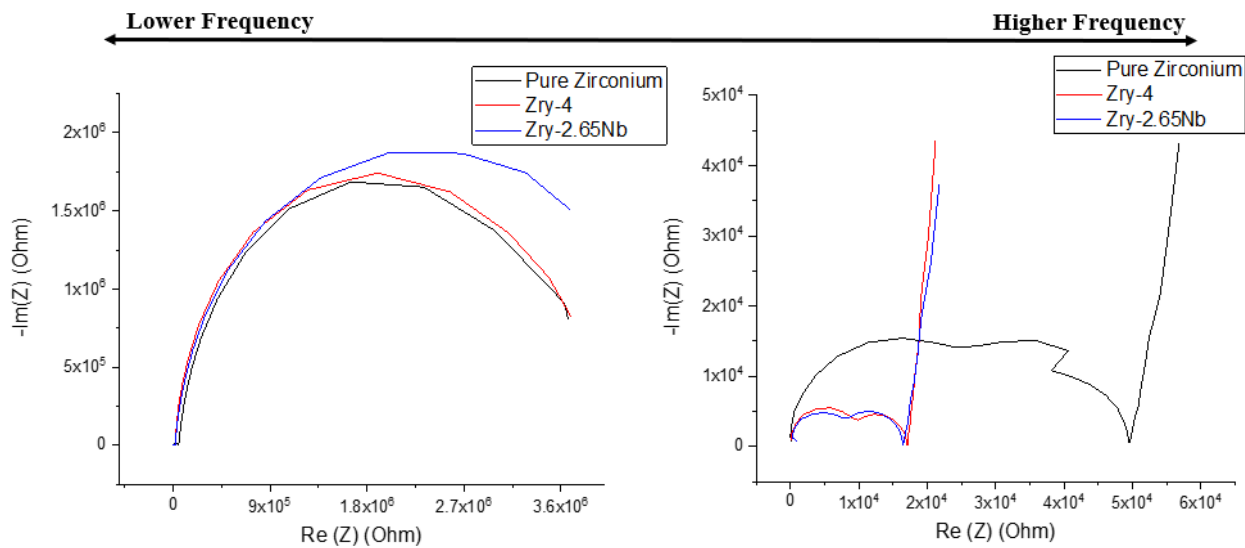
Figure A.9   Unfitted Nyquist plots for varying alloys in KOH.
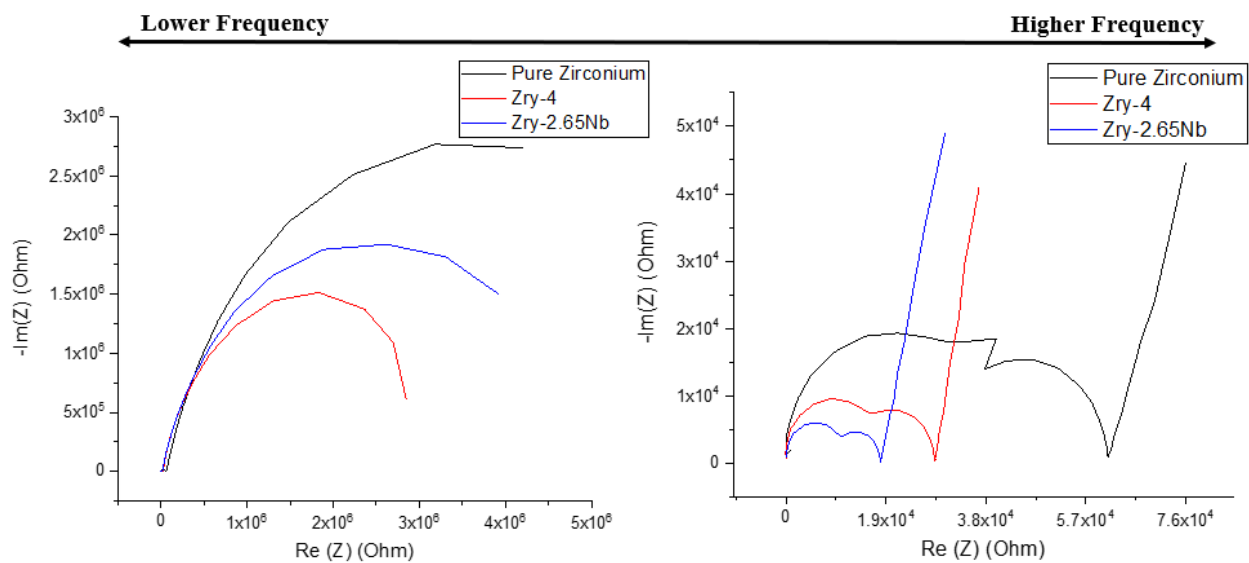
Figure A.10   Unfitted Nyquist plots for varying alloys in LiOH.
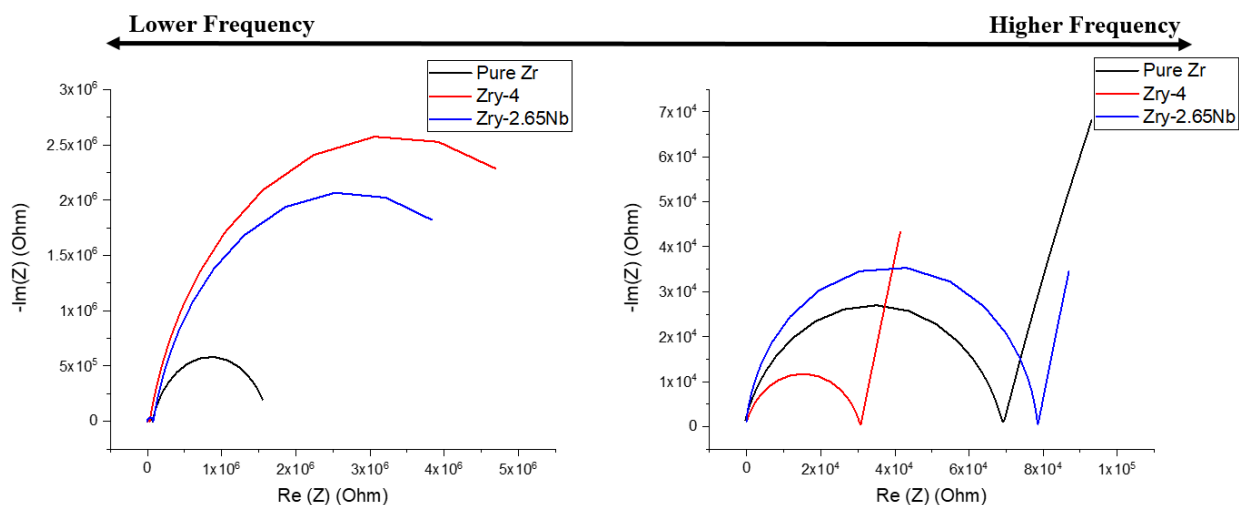
Figure A.11   Fitted Nyquist plots for varying alloys in DI-Water.
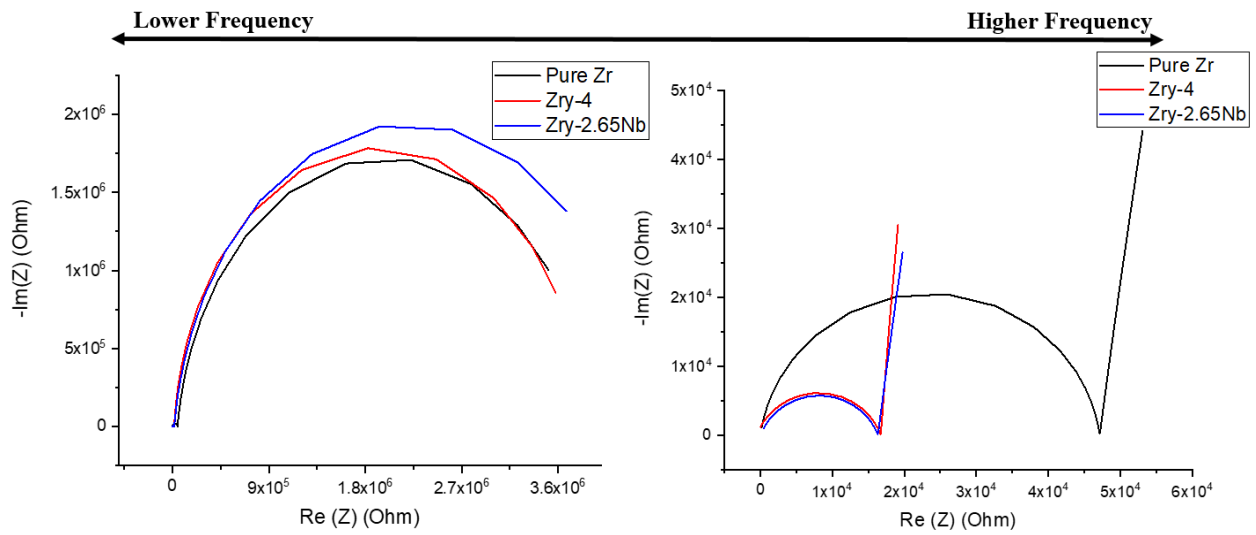
Figure A.12 Fitted Nyquist plots for varying alloys in KOH.
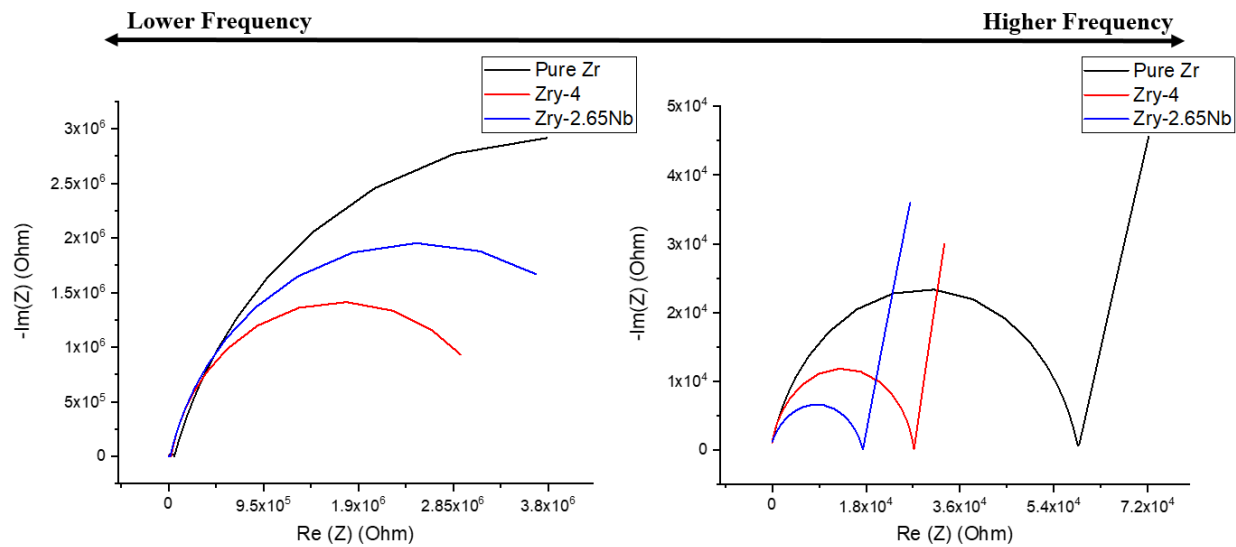
Figure A.13 Fitted Nyquist plots for varying alloys in LiOH.
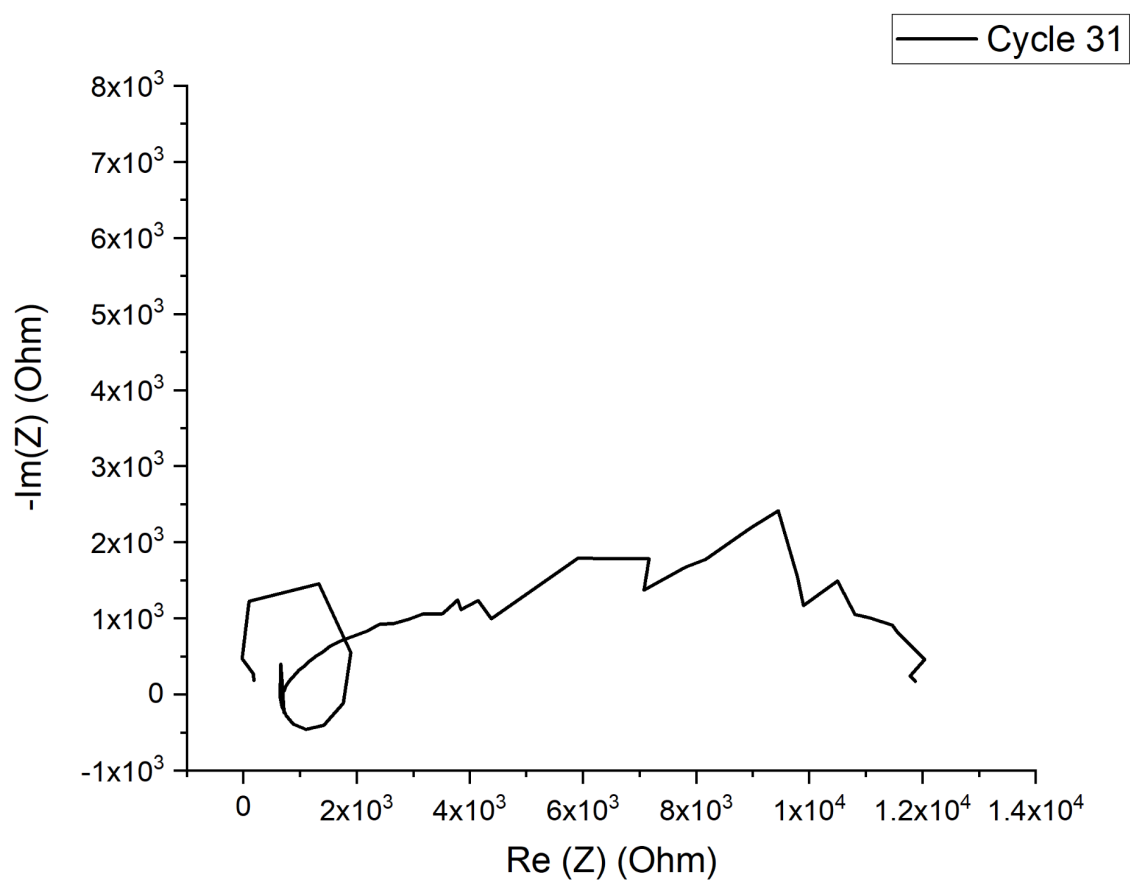
Figure A.14   Nyquist plot for Zry-4 high temperature sample at last cycle.
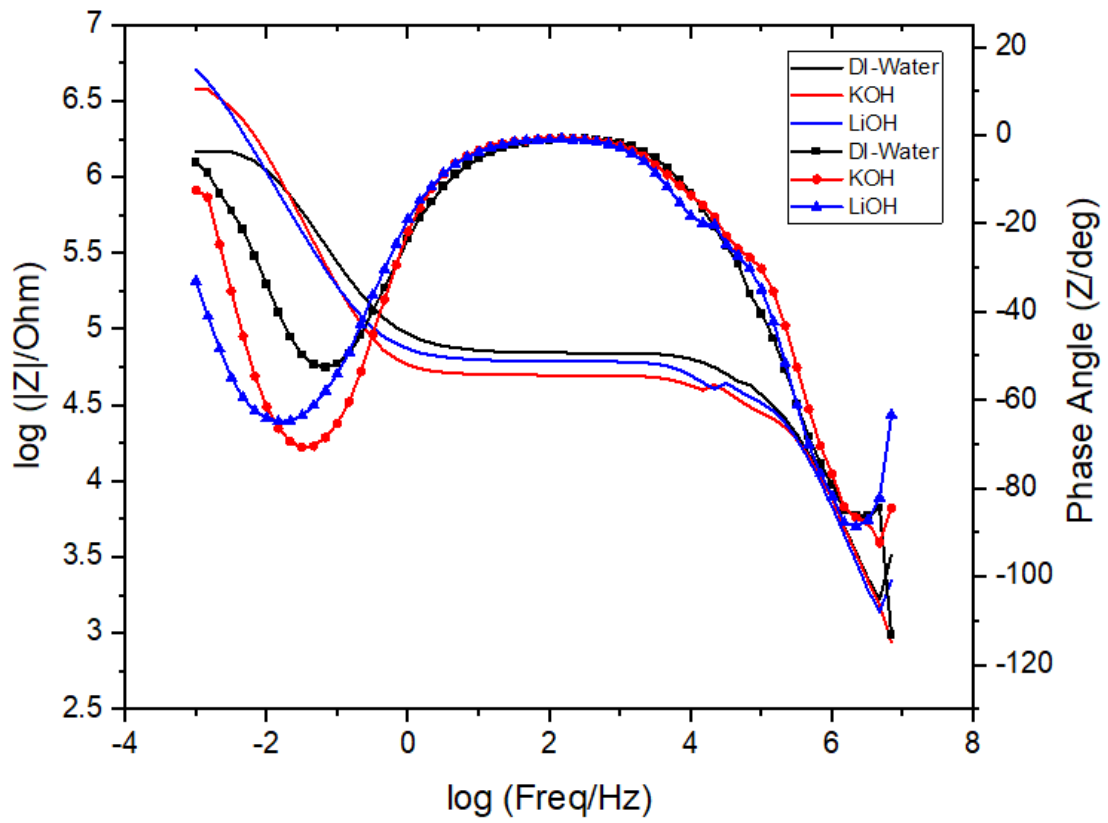
Figure A.15   Bode plot for Pure Zirconium in varying electrolytes.
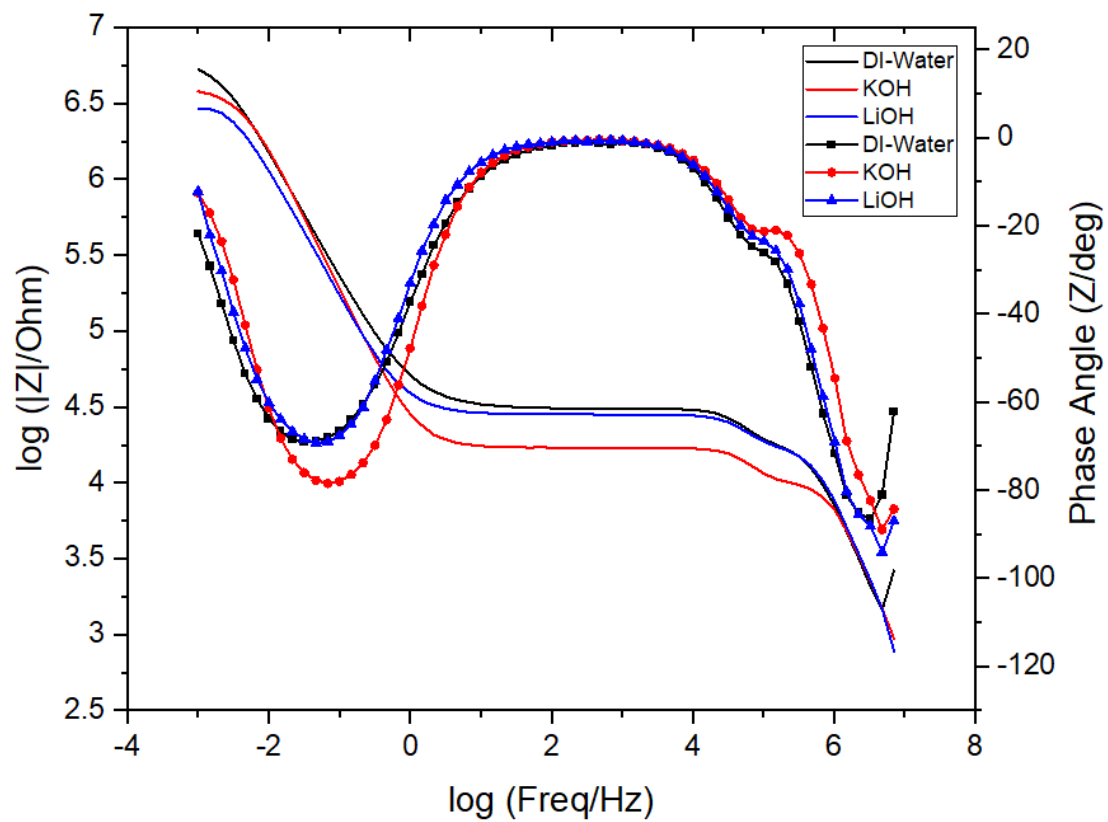
Figure A.16   Bode plot for Zry-4 in varying electrolytes.
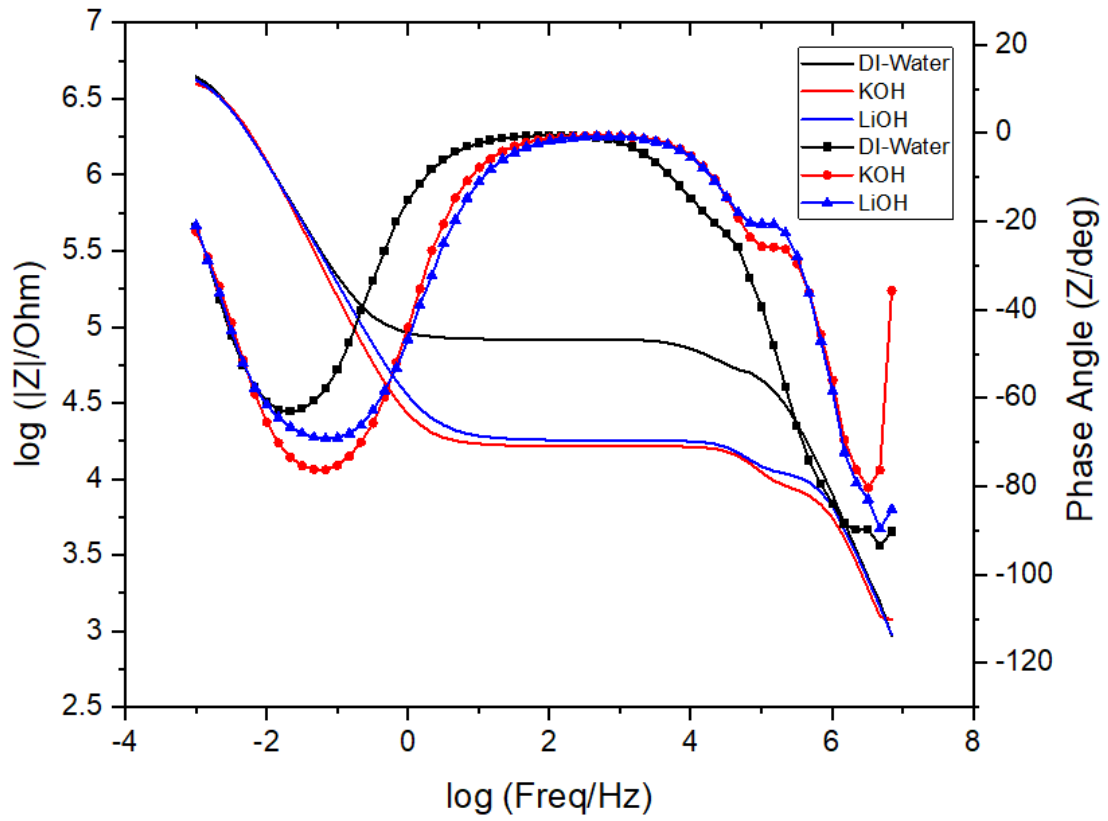
Figure A.17   Bode plot for Zry-2.65Nb in varying electrolytes.